ORNL/TM-2024/3389

Evaluation of XCT for Matrix Density Measurement of Particle Fuel Forms

Grant W. Helmreich
Katherine I. Montoya
John D. Hunn

May 2024

Approved for public release.
Distribution is unlimited.

OAK RIDGE National Laboratory

ORNL IS MANAGED BY UT-BATTELLE LLC FOR THE US DEPARTMENT OF ENERGY

ORNL/TM-2024/3389

Nuclear Energy and Fuel Cycle Division

EVALUATION OF XCT METHODS FOR MATRIX DENSITY MEASUREMENT OF PARTICLE FUEL FORMS

Grant W. Helmreich
Katherine I. Montoya
John D. Hunn

May 2024

Work sponsored by
US DEPARTMENT OF ENERGY
Office of Nuclear Energy—Advanced Reactor Technologies
under the
Advanced Gas Reactor Fuel Development and Qualification Program

Prepared by
OAK RIDGE NATIONAL LABORATORY
Oak Ridge, TN 37831
managed by
UT-BATTELLE LLC
for the
US DEPARTMENT OF ENERGY
under contract DE-AC05-00OR22725

CONTENTS

LIST OF FIGURES

LIST OF TABLES

ABBREVIATIONS

3D	three-dimensional
AGR	Advanced Gas Reactor Fuel Development and Qualification Program
IPyC	inner pyrolytic carbon
ORNL	Oak Ridge National Laboratory
TRISO	tristructural isotropic
UCO	uranium carbide/uranium oxide
XCT	x-ray computed tomography

ABSTRACT

Particle fuel forms generally consist of a dispersion of fuel, such as tristructural isotropic (TRISO) particles, within a refractory matrix (e.g., graphite or silicon carbide). The density of matrix materials for particle fuel forms is of interest for modeling fuel form strength and thermal properties and may be specified as a quality control parameter, depending on reactor design. Some of the uncertainty associated with traditional, manual approaches can be eliminated by performing x-ray computed tomography (XCT) on the fuel forms and applying image processing methods to generate a precise count of the number of particles. This also removes the need to include determination of particle count within each individual fuel form during fabrication. Unfortunately, reconstruction artifacts from high-Z uranium-bearing kernels prevent accurate measurement of individual particle volumes using this approach, so the use of mean particle mass and volume are still necessary for computation of average fuel form matrix density. This method of using XCT to count particles in individual fuel form for determination of average matrix density was applied to three archived compacts from the Advanced Gas Reactor Fuel Development and Qualification (AGR)-1 campaign [1], four archived compacts with uranium carbide/uranium oxide (UCO) TRISO from the AGR-2 campaign [2], and three archived UO_2-TRISO compacts from the AGR-2 campaign [3]. The resulting density values were compared with those previously reported, showing slight changes due to uncertainties in the previously used number of particles in each of these cylindrical, graphite matrix compacts.

1. XCT IMAGING OF AGR-1 COMPACTS

Three AGR-1 Baseline compacts were randomly selected from the existing material archive at Oak Ridge National Laboratory (ORNL). These compacts were fabricated for the first irradiation campaign of the AGR Program. Each compact contained a nominal charge of 4.86 g of overcoated particles as well as two 0.40 g matrix-only end caps [1]. Compacts were individually imaged in a Zeiss Versa 620 XCT system. The imaging parameters selected for the compacts were a source voltage of 160 kV, a source power of 25 W, a source-to-sample distance of 200 mm, and a sample-to-detector distance of 260 mm with the 0.4× detector objective, resulting in a voxel edge dimension of 14.9 μm. A total of 3201 radiographs were acquired for each compact, evenly distributed over 360 degrees of rotation about the cylinder axis, with a 15 s exposure for each radiograph, resulting in a 16 h scan time per compact.

These imaging conditions were selected to optimize image quality for the complex system of exceptionally high-Z, and thus high attenuation, uranium-bearing kernels in close proximity to exceptionally low-Z graphitic matrix, which must be segregated from the surrounding air. High source voltage was selected to ensure at least some transmission of x-rays through the kernels, thereby reducing image artifacts during reconstruction. The source-to-sample and sample-to-detector distances were also maximized to reduce the prevalence of scattered x-rays reaching the detector. The same image magnification with improved x-ray counts could have been achieved by moving the source and the detector closer to the sample; however, scattered x-rays from the high-Z kernels resulted in blurring of the nearby matrix–air interface. This deleterious effect of x-ray scattering was reduced by increasing the sample-to-detector distance, which required a matching increase in the source-to-sample distance to maintain magnification. Example cross-sectional images of one of the AGR-1 compacts obtained via three-dimensional (3D) tomographic reconstruction from the radiographs are given in Figure 1.

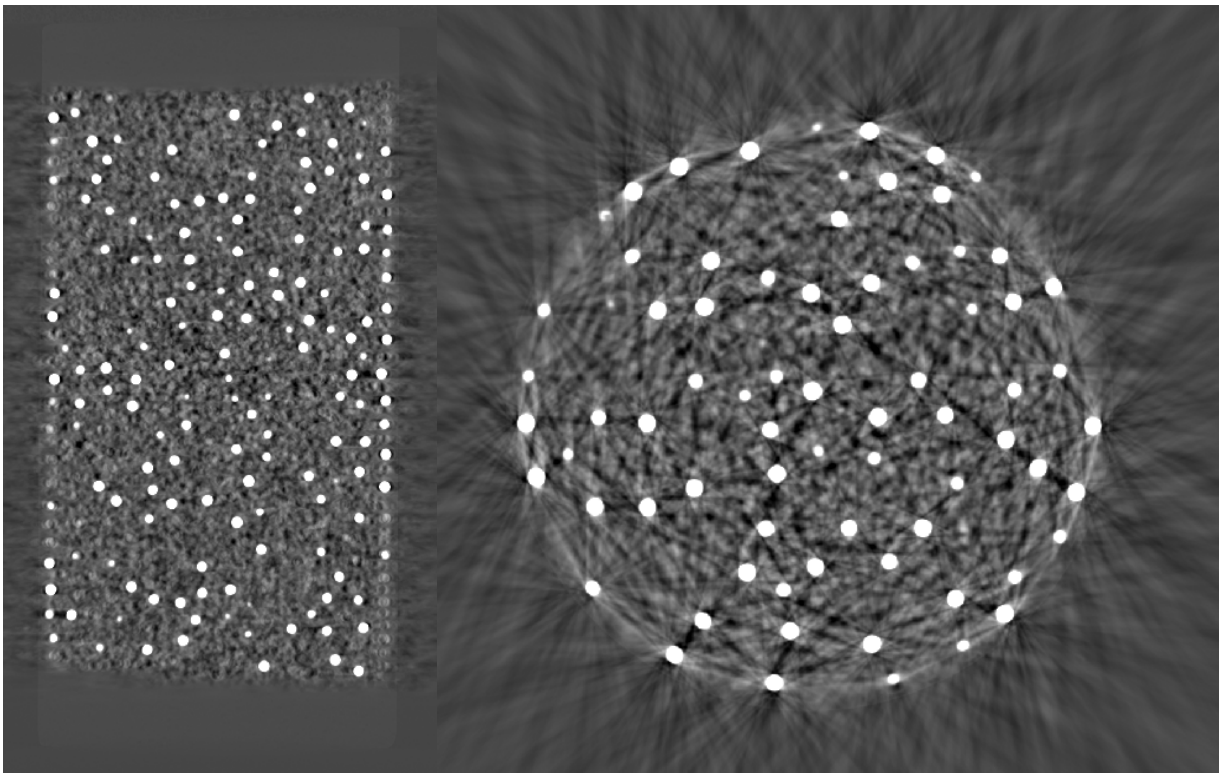

Figure 1. Axial and radial cross-sections of LEU01-46T-Z68 acquired using XCT.

2. PROCESSING OF AGR-1 XCT DATA

The reconstructed XCT images generated for each compact consisted of a 3D array approximately 2000 voxels in each dimension with 16-bit intensity depending on local attenuation of x-rays. Previously developed MATLAB scripts for processing XCT images of TRISO-bearing pebbles [4] were modified for use with the compact XCT data. These scripts identify particle positions based on kernel centroids, segment the fuel form matrix from the surrounding air, and calculate parameters of interest for each identified particle such as local packing fraction and nearest neighbor distances.

Identification of kernels within the XCT images is relatively straightforward due to their strong attenuation of x-rays. The primary challenge is avoiding reconstruction artifacts, notably bright streaks between kernels. These artifacts are especially prevalent near the outer surface of the fuel form, and they are typically of a slightly lower intensity than the kernels themselves. Therefore, selecting a higher segmentation threshold is generally sufficient to avoid including them in the kernel mask. Since measurement of kernel volume is not necessary, precisely finding the edge of each kernel is not critical. After initial segmentation of kernels, potential failures in the segmentation were identified by looking for deviations in kernel size or shape that might indicate inclusion of small artifacts or consolidation of multiple kernels into a single object due to the bright streaks connecting them. The refined set of segmented kernels was then processed to determine individual parameters, including position within the compact, nearest neighbor distances, and local packing fraction based on the nominal particle volume and the surrounding matrix volume within each particle's zone of control as determined by a watershed segmentation. The details of this process can be found elsewhere [4]. Although these parameters are not the focus of this report, they are of general interest in understanding variations in particle packing as a function of position within the compact and are therefore reported in Appendix A.

Segmentation of the compact matrix from the surrounding air was substantially more difficult for the AGR compacts than it was for the pebbles for which this method was originally developed due to their differing geometries. A combination of bright streaks and dark patches in the coatings and matrix surrounding the kernels (see Figure 1) due to the overlapping obstruction of multiple nearby high-Z objects was present in both fuel forms; however, the outer fuel-free zone in pebbles provided a buffer zone of several millimeters between the outermost kernels and the edge of the matrix, which was sufficient to prevent these artifacts from affecting imaging of the matrix/air interface. In the AGR compacts, particles are present up to the outer radial edge, resulting in significant disruption of the matrix/air interface image. This challenge was resolved by using the top and bottom portions of the compacts, which consisted of matrix only, to determine the overall compact volume by assuming that the compacts were right cylinders. The fuel-free zones above and below the compact were segmented separately, and the shift in centroid position between the two was used to account for any tilt in the compact as mounted in the XCT system. The side wall coordinates of the compact between the top and bottom sections were interpolated based on the compact cross sections measured for the two end caps combined with a lateral shift to account for any measured compact tilt. The results of this approach for one compact are shown in Figure 2. In this segmented tomogram, the matrix (blue) in the vicinity of the kernels (red) is mottled due to the complex pattern of reconstruction artifacts generated by the high-Z kernels. These artifacts can be seen to extend somewhat laterally to the left and right of the compact. In contrast, the matrix in the endcaps at the top and bottom of the compact has a uniform appearance.

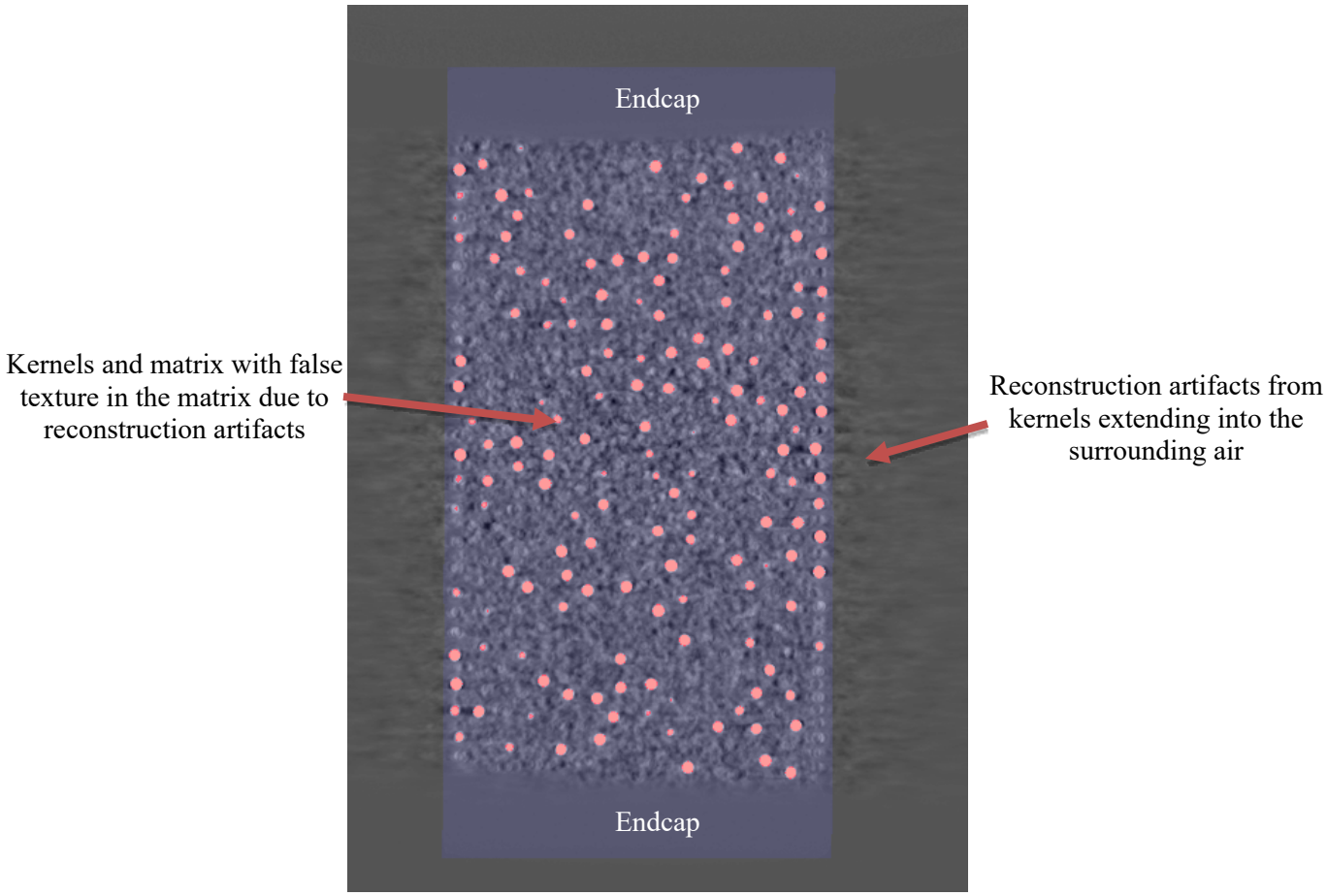

Figure 2. Segmented axial cross-section from XCT of LEU01-46T-Z68 with kernels (red) and matrix (blue).

After image processing was completed, the mass of matrix in each compact was calculated by subtracting the average particle mass times the number of kernels observed from the total compact mass. The volume of matrix in each compact was similarly calculated by subtracting the average particle volume times the number of kernels observed from the total compact volume. Average matrix density for each compact was then calculated by dividing the calculated matrix mass by the calculated matrix volume.

3. XCT IMAGING AND PROCESSING OF AGR-2 COMPACTS

Based on the results from the AGR-1 compacts, in which kernels could be readily segmented and counted but segmentation of graphitic matrix and surrounding air was more difficult, seven compacts from AGR-2 (four with UCO kernels from LEU09 and three with UO_2 kernels from LEU11) were imaged using much more rapid scanning conditions optimized for rapid identification of kernel positions. As with the AGR-1 compacts, AGR-2 compacts were individually imaged in a Zeiss Versa 620 XCT system. However, for the AGR-2 compacts, imaging parameters were set to a source voltage of 100 kV, source power of 14 W, source-to-sample distance of 60 mm, and sample-to-detector distance of 230 mm with the flat panel detector, resulting in a voxel dimension of 15.50 μm. A total of 201 radiographs were acquired for each compact, evenly distributed over 360° of rotation about the axis, with a 0.1 s exposure for each radiograph, resulting in a 3.5 min scan time per compact. Example tomographic cross-sectional images from one of the AGR-2 compacts imaged using these conditions are shown in Figure 3.

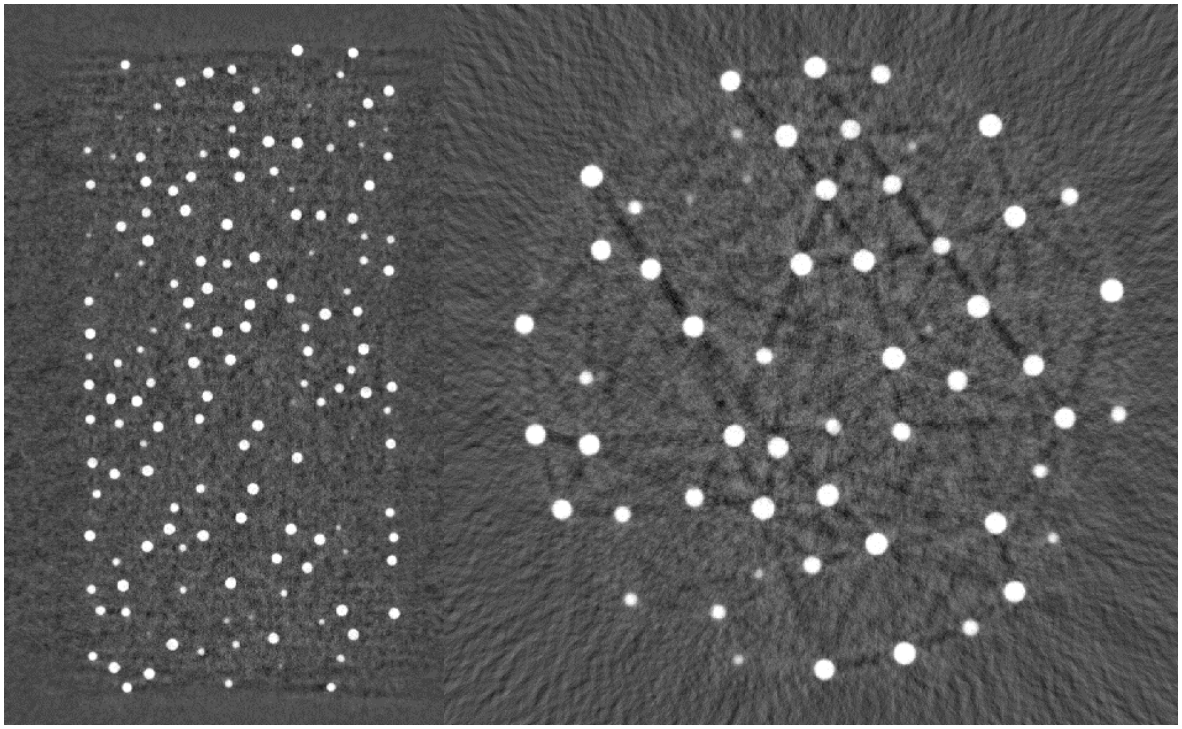

Figure 3. Axial and radial cross-sections of LEU09-OP2-Z069 acquired using XCT.

Processing of the AGR-2 compact XCT data was performed in the same manner as the AGR-1 compact XCT data, except that no effort was made to segment the compact matrix from the surrounding air. Therefore, manually measured fuel form volumes based on caliper measurements were used exclusively for AGR-2 compact density calculations along with the exact particle count from XCT.

For the purposes of calculating local particle packing fractions (reported for general information in Appendix B and Appendix C), approximate compact boundaries were determined by taking the image of

all the kernels within the compact, dilating that image by the mean particle radius minus the mean kernel radius, then taking the convex hull of the resulting image. This effectively sets the assumed boundaries of the compact based on the known fact that particles along the walls of the compact are very close to the compact edge.

4. RESULTS AND COMPARISON TO PREVIOUS MATRIX DENSITY MEASUREMENTS

Matrix density was not specifically determined during the acceptance testing of the AGR-1 fuel compacts because it was not specified in the AGR-1 Fuel Specification [5]. However, data acquired and reported in the acceptance test data compilations was sufficient to estimate the average matrix density of the compacts in each of the AGR-1 compact lots. After fabrication, the dimensions and mass of each AGR-1 compact were measured. Compact height was measured using a vertical height gauge, and compact diameter was measured twice near the top, twice near the middle, and twice near the bottom. These dimensional measurements allow for a calculation of individual compact volume with the assumption that the compacts are nearly perfect right cylinders. This is a reasonable assumption given that right cylinder dies were used to press the compacts and shrinkage in either the axial or radial direction during carbonization and heat treatment after pressing were both nearly symmetric (i.e., final compacts did not significantly vary from their original right cylinder shape). Radiography for defective inner pyrolytic carbon (IPyC) analysis of particles from twelve deconsolidated AGR-1 Baseline compacts counted a total of 49,735 particles, which equates to 4145 particles per compact on average [1]. Using the average number of particles per compact, the mean mass of particles per compact was estimated to be 3.013 g from the reported mean particle mass of 7.269E-4 g [6]. Similarly, the mean volume of particles per compact was estimated to be 1.098 cm^3 using the mean particle envelope volume of 2.648E-4 cm^3 [6]. Taken together, these values allowed a calculation of an overall mean matrix density for the AGR-1 Baseline compact lot of 1.292 g/cm^3 by subtracting mean particle mass and volume from the mean of the reported compact masses and volumes for all compacts in the lot, of 5.482 g and 3.008 cm^3 [6]. While not technically accurate because the number of particles varied from compact to compact, Table 1 shows an estimated matrix density for the three selected AGR-1 compacts using the individual masses and volumes for each compact coupled with the average data for particle mass and volume per AGR-1 Baseline compact based on 4145 particles per compact on average.

Table 1. Measured parameters and calculated matrix values for three AGR-1 Baseline compacts assuming 4145 particles per compact.

Compact ID	Compact Mass (g)	Compact Length (mm)	Mean Compact Diameter (mm)	Compact Volume (cm^3)	Matrix Mass (g)	Matrix Volume (cm^3)	Matrix Density (g/cm^3)
LEU01-46T-Z03	5.4757	24.857	12.41	3.006	2.463	1.908	1.290
LEU01-46T-Z47	5.4802	25.041	12.37	3.009	2.467	1.911	1.291
LEU01-46T-Z68	5.4756	24.928	12.37	2.993	2.463	1.895	1.299

Table 2 provides results for individual compact matrix density for the three AGR-1 compacts imaged with XCT. Since uranium kernels were easy to segment in the XCT images, the actual number of particles in each compact were determined with XCT and used to better estimate the total particle volume and particle mass. Application of XCT for direct measurement of compact volume was less straightforward due to the noted challenges in segmenting the compact from the surrounding air in the vicinity of particles through the midsection of the compact. Therefore, matrix density was calculated using both the external dimensions that were previously measured manually [1] and the estimation from the XCT images discussed in Section 2 to allow for a comparison of the two methods. The compact volumes measured by

XCT were found to be within 2% of the values calculated from caliper and height gauge measurement, but a discrepancy in two of the three compact volumes was enough to significantly impact the calculated matrix density for those compacts. The XCT volume for LEU01-46T-Z47 was particularly low compared with the manual measurements, and the difference suggests that the XCT edge detection was off by more than 0.1 mm, which is more than 10× greater than the uncertainty in the caliper measurements, which appear to provide the more reliable value.

The error in the XCT determined volumes is likely primarily due to error in segmentation of the radial boundary of the the compact edge. At that edge there is a gradient in image intensity and a combination of segmentation algorithms and operator judgment is necessary to determine the thresholds used to define where the boundary lies within the gradient. The difference between the volume results from XCT and caliper measurements would be resolved by shifting the radial boundary identified by the XCT image anaylsis algorithm outward by ~2-3 voxels, which is still within the range of the intensity gradient. However, doing so would not provide an independent measure of volume by XCT as it would remain dependent on the caliper determined volume used for calibration of the algorithm. In future work, manually measured compact dimensions for a reference set of compacts could be used to calibrate the image segmentation algorithm such that it could be used to accurately measure the volume of other compacts of similar geometry.

Table 2. Revised AGR-1 matrix density calculations using XCT data for actual particle count.

				External Dimensions		XCT Volume Segmentation	
Compact ID	Number Particles	Total Mass Particles (g)	Total Volume Particles (cm^3)	Compact Volume (cm^3)	Matrix Density (g/cm^3)	XCT Volume (cm^3)	Matrix Density (g/cm^3)
LEU01-46T-Z03	4155	3.020	1.100	3.006	1.288	2.966	1.317
LEU01-46T-Z47	4143	3.012	1.097	3.009	1.291	2.950	1.333
LEU01-46T-Z68	4131	3.003	1.094	2.993	1.302	2.996	1.300

On average the matrix density calculated using the manually determined external dimensions and the actual number of particles (Table 2) did not change compared to the calculation using the average number of particles (Table 1). However, a slight impact can be seen for individual compact matrix densities that was congruent with the relatively minor fractional variation in the actual particle count from the average. LEU01-46T-Z03 had a 0.24% higher-than-average number of particles, and thus showed a slight decrease in calculated matrix density when using the correct particle count. Conversely, LEU01-46T-Z68 had a 0.34% lower-than-average number of particles, and thus had a slight increase in calculated matrix density when using the correct particle count. Finally, LEU01-46T-Z47 had nearly the average number of particles and saw virtually no change in calculated matrix density. While all compacts were fabricated using the same overcoated charge weight of 4.86 g, there were two factors noted during fabrication which caused variation in particle loading over time [1]. First, the overcoated particles were not riffled into charges, so natural stratification based on overcoated particle size impacted random sampling. Second, some evaporation of methanol from the overcoated particles occurred over time, gradually reducing the average overcoated particle mass.

The overcoated particle stratification which was observed in AGR-1 was rectified in AGR-2 by the use of rotary riffling to produce randomly generated charges of overcoated particles for compacting [2, 3]. Matrix density was added to the AGR fuel specification for the AGR-2 irradiation campaign [7]. Therefore, a procedure was developed to determine matrix density for AGR-2 compacts using the overcoated charge weight and the mean overcoated particle mass to calculate the number of particles in each compact. However, the issue of overcoated particles losing mass by drying over time persisted, and

it was noted in the compact data compilations that the measured mean overcoated particle weight appeared to be lower than it was in the weighed overcoated particle charges due to greater weight loss from methanol evaporation compared to the compact charges [2, 3]. As a result, the average number of particles in AGR-2 UCO compacts (3176) and AGR-2 UO_2 compacts (1543), as determined by radiography during defective IPyC examination, were low compared to the target loadings of 3200 and 1566 particles per compact, respectively.

This slight 0.4%–1.0% error in the calculation of the number of particles in each compact resulted in a corresponding 0.2%–0.5% error in the calculated matrix density for each AGR-2 UCO compact (see Table 3 and Table 4). For the AGR-2 UO_2 compacts, a 0.8%–1.9% error in the calculated number of particles led to a 0.2%–0.6% error in the calculated matrix density (see Table 5 and Table 6). The smaller relative impact on matrix density from counting error in the UO_2 compacts was related to the lower UO_2 TRISO particle packing fraction, and thus, higher fraction of matrix weight and volume versus particle weight and volume in the UO_2 compacts. In every AGR-2 compact imaged by XCT the actual number of particles was lower than the calculated number of particles based on overcoated charge weight and close to the average number of particles per compact determined by radiography during defective IPyC examination, as expected, given the error from using an erroneously low overcoated particle weight when riffling the compacting charge.

Table 3. Matrix density calculation for selected AGR-2 UCO compacts using overcoated particle charge mass and mean overcoated particle mass to calculate the number of particles in each compact [2].

Compact ID	Number Particles	Mass Particles (g)	Volume Particles (cm^3)	Compact Volume (cm^3)	Matrix Density (g/cm^3)
LEU09-OP2-Z069	3200	3.303	1.098	2.990	1.597
LEU09-OP2-Z102	3200	3.302	1.098	2.980	1.590
LEU09-OP2-Z139	3200	3.302	1.098	2.975	1.589
LEU09-OP2-Z165	3200	3.302	1.098	2.975	1.591

Table 4. Matrix density calculation for selected AGR-2 UCO compacts using actual number of particles as counted by XCT.

Compact ID	Number Particles	Mass Particles (g)	Volume Particles (cm^3)	Compact Volume (cm^3)	Matrix Density (g/cm^3)
LEU09-OP2-Z069	3186	3.288	1.093	2.990	1.600
LEU09-OP2-Z102	3167	3.268	1.086	2.980	1.598
LEU09-OP2-Z139	3184	3.286	1.092	2.975	1.593
LEU09-OP2-Z165	3170	3.271	1.087	2.975	1.599

Table 5. Matrix density calculation for selected AGR-2 UO_2 compacts using overcoated particle charge mass and mean overcoated particle mass to calculate the number of particles in each compact [3].

Compact ID	Number Particles	Mass Particles (g)	Volume Particles (cm^3)	Compact Volume (cm^3)	Matrix Density (g/cm^3)
LEU11-OP2-Z045	1566	2.289	0.697	2.978	1.687
LEU11-OP2-Z074	1567	2.291	0.697	2.962	1.678
LEU11-OP2-Z198	1567	2.291	0.697	2.977	1.665

Table 6. Matrix density calculation for selected AGR-2 UO_2 compacts using actual number of particles as counted by XCT.

Compact ID	Number Particles	Mass Particles (g)	Volume Particles (cm^3)	Compact Volume (cm^3)	Matrix Density (g/cm^3)
LEU11-OP2-Z045	1554	2.272	0.692	2.978	1.691
LEU11-OP2-Z074	1537	2.247	0.684	2.962	1.687
LEU11-OP2-Z198	1545	2.259	0.688	2.977	1.672

5. CONCLUSIONS AND RECOMMENDATIONS

The method presented herein represents an iterative improvement on the previous approach for determination of mean matrix density in compacts. One of the sources of uncertainty in the former approach was a result of using either the average number of particles for each compact, as was done for AGR-1, or the estimated number of particles based on overcoated particle charge weight and the mean overcoated particles mass, as was done for AGR-2. This source of uncertainty was effectively removed by counting individual kernels in the XCT image. The uncertainty due to using average particle mass and average particle volume to subtract from the total compact mass and volume remains but is relatively minor if the particles within the compact are sampled from the particle composite using an appropriately random method (e.g., riffling) and are sufficiently numerous that the average values apply. With several thousand particles in a compact, any deviation from using the mean values will be quite minor.

While the XCT provided a more accurate particle count for each compact, it was less effective in determining the compact volume due to the challenges of accurately segmenting matrix from the surrounding air when many high-Z kernels in the vicinity introduce reconstruction artifacts. Although compact volume could be measured from the XCT data using interpolation between the top and bottom portions of the compact, this approach was less accurate than the measurement of compact height and radius at multiple points with calipers due to the uncertainty in defining the radial edge of the compacts by thresholding. Refining the XCT approach would require improved reconstruction algorithms capable of handling the very challenging problem of large shifts in x-ray attenuation over small distances. More effective XCT imaging for volume analysis has been obtained for pebble fuel forms because of the fuel-free, matrix-only zone associated with this fuel form design [4].

Considering that the segmentation of the matrix for determination of compact volume was found not to improve accuracy over traditional caliper measurements for the AGR-1 compacts imaged, the imaging conditions used for the AGR-2 compacts were optimized to produce an accurate count of the number of kernels in each compact within a 3.5 min scan time, which demonstrates that the XCT method of counting particles would be feasible in statistical quality control applications. The XCT approach also has substantial benefit in determination of compact matrix density in that it provides a discrete value for each compact while being independent of the fabrication process. In the case of the AGR-1 and AGR-2 compacts analyzed in this study, the calculated matrix density was only slightly affected by the use of the actual number of particles in each compact. However, in a scaled-up industrial fuel fabrication process, for which the controls used within the AGR program may not propagate well at higher throughput, a rapid method to nondestructively determine the number of particles in each compact independently of fabrication parameters may be more important for accurate calculation of matrix density. It is important to note that it will likely not be necessary to measure matrix density in every compact as long as a random sample of compacts is sufficient in number to obtain a mean and standard deviation representative of the entire lot. The application of XCT to support matrix density measurement would be strengthened if it was also being used for other fuel form characterization. Such is the case for pebble fuel forms, in which the

fuel-free zone may need to be monitored, or in cases where the number of particles per compact must be verified for nuclear material safeguards requirements.

6. REFERENCES

[1] J. Hunn, F. Montgomery and P. Pappano, "Data Compilation for AGR-1 Baseline Compact Lot LEU01-46T-Z," ORNL\TM-2006\507, Oak Ridge National Laboratory, Oak Ridge, 2006.

[2] J. Hunn, F. Montgomery and P. Pappano, "Data Compilation for AGR-2 UCO Variant Compact Lot LEU09-OP2-Z," ORNL\TM-2010\017, Oak Ridge National Laboratory, Oak Ridge, 2010.

[3] J. Hunn, F. Montgomery and P. Pappano, "Data Compilation for AGR-2 B&W UO2 Compact Lot LEU11-OP2-Z," ORNL\TM-2010\055, Oak Ridge National Laboratory, Oak Ridge, 2010.

[4] G. Helmreich, J. Hunn, D. Brown and B. Blamer, "New method for analysis of x-ray computed tomography scans of TRISO fuel forms," *Nuclear Engineering and Design,* vol. 357, 2020.

[5] C. Barnes, "AGR-1 Fuel Product Specification and Characterization and Guidance," EDF-4380, Rev 8, Idaho National Laboratory, Idaho Falls, ID, 2006.

[6] J. Hunn and R. Lowden, "Data Compilation for AGR-1 Baseline Coated Particle Composite LEU01-46T," ORNL\TM-2006\019, Oak Ridge National Laboratory, Oak Ridge, 2006.

[7] C. Barnes, "AGR-2 Fuel Specification," SPC-923 Rev 3, Idaho National Laboratory, Idaho Falls, ID, 2009.

APPENDIX A: PARTICLE DATA FROM AGR-1 BASELINE COMPACT XCT SCANS

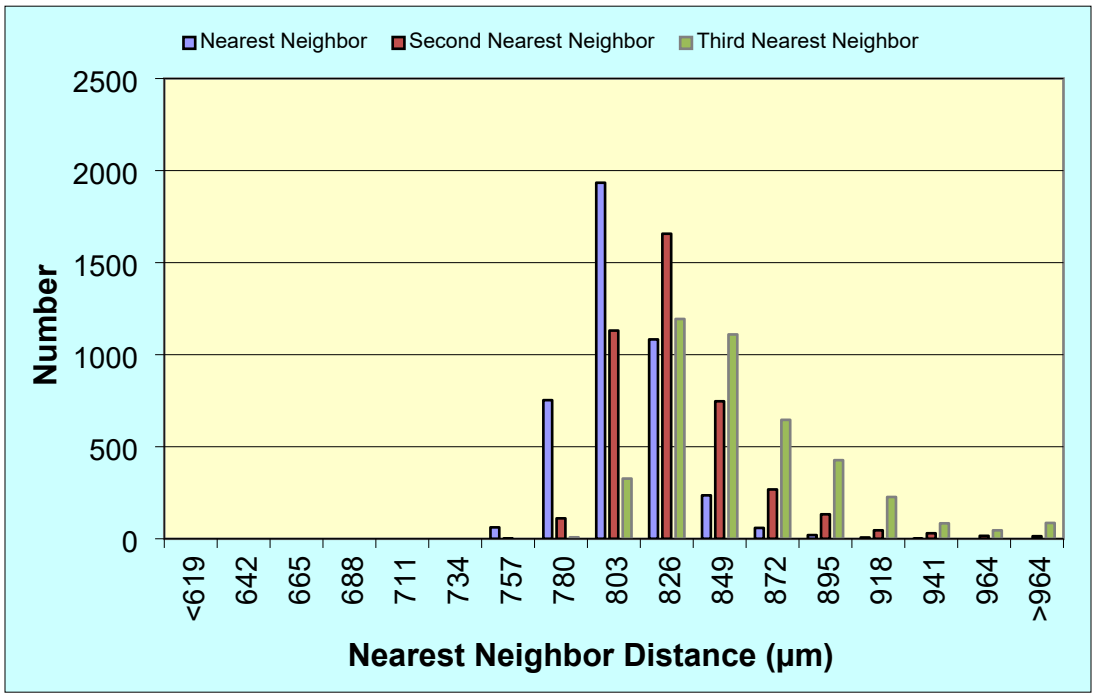

Figure 4. Nearest-neighbor distances for particles in LEU01-46T-Z03.

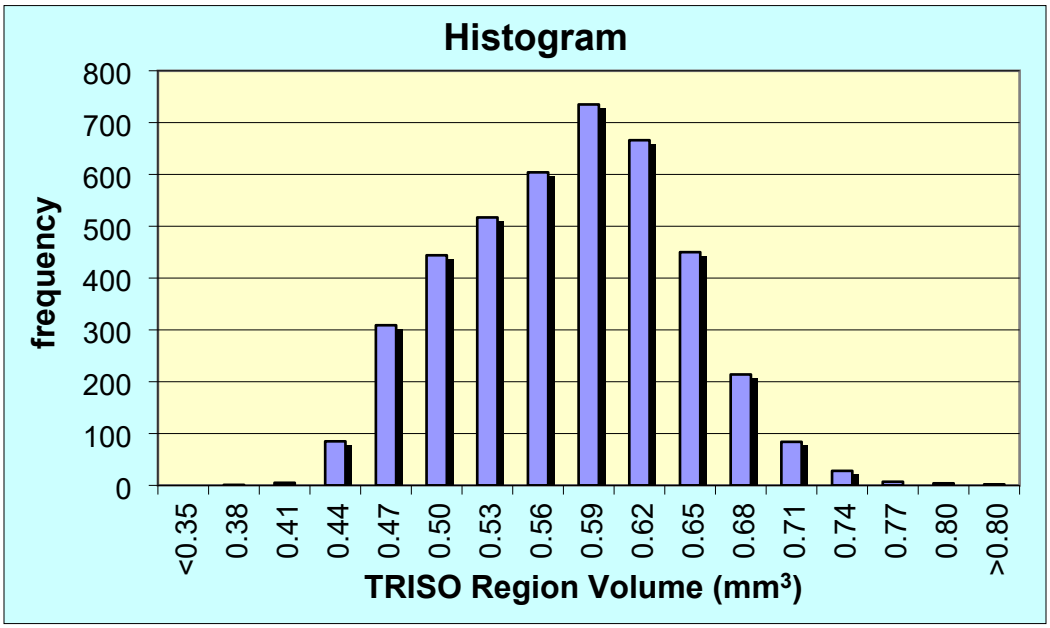

Figure 5. Region volumes of particles and surrounding matrix for particles in LEU01-46T-Z03.

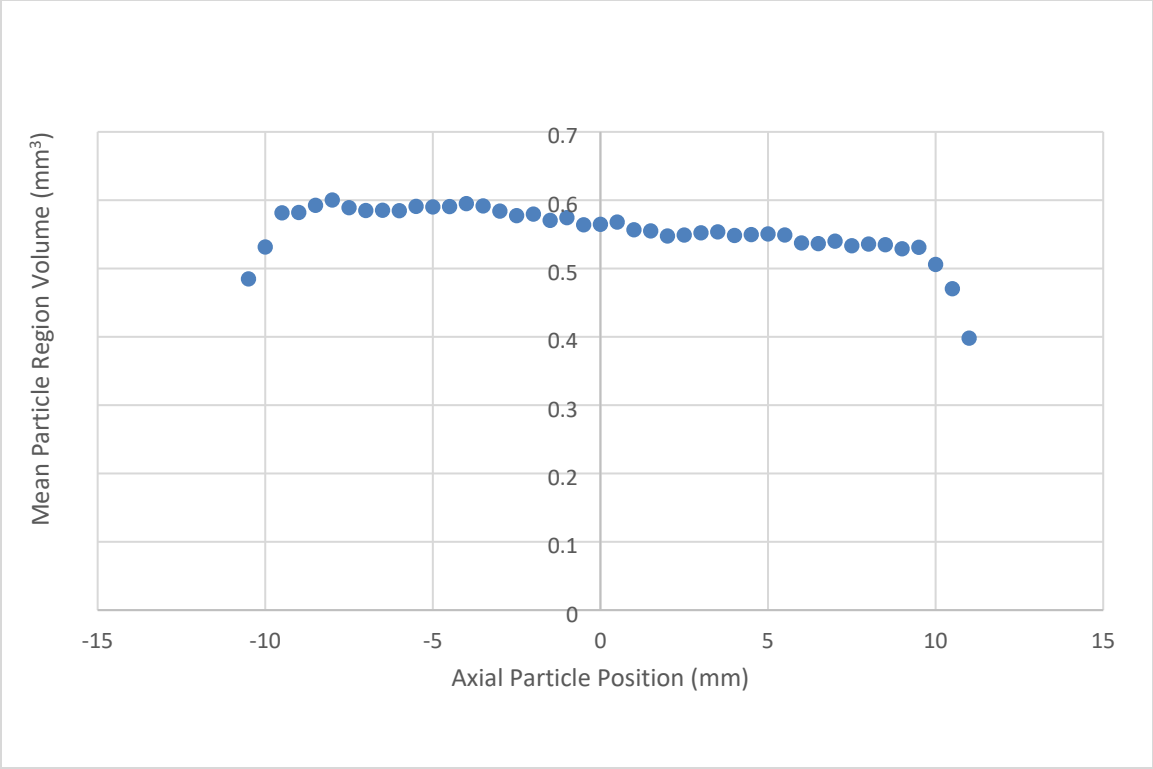

Figure 6. Mean region volume as a function of axial position within compact LEU01-46T-Z03.

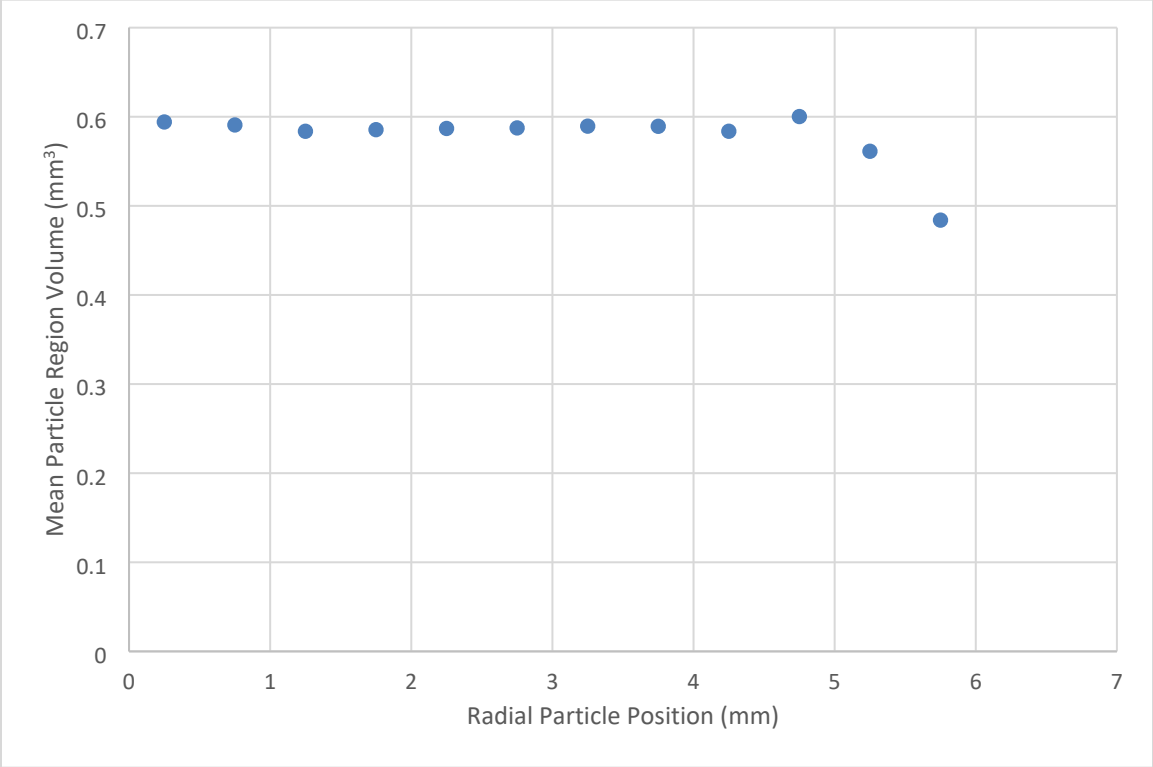

Figure 7. Mean region volume as a function of radial position within compact LEU01-46T-Z03.

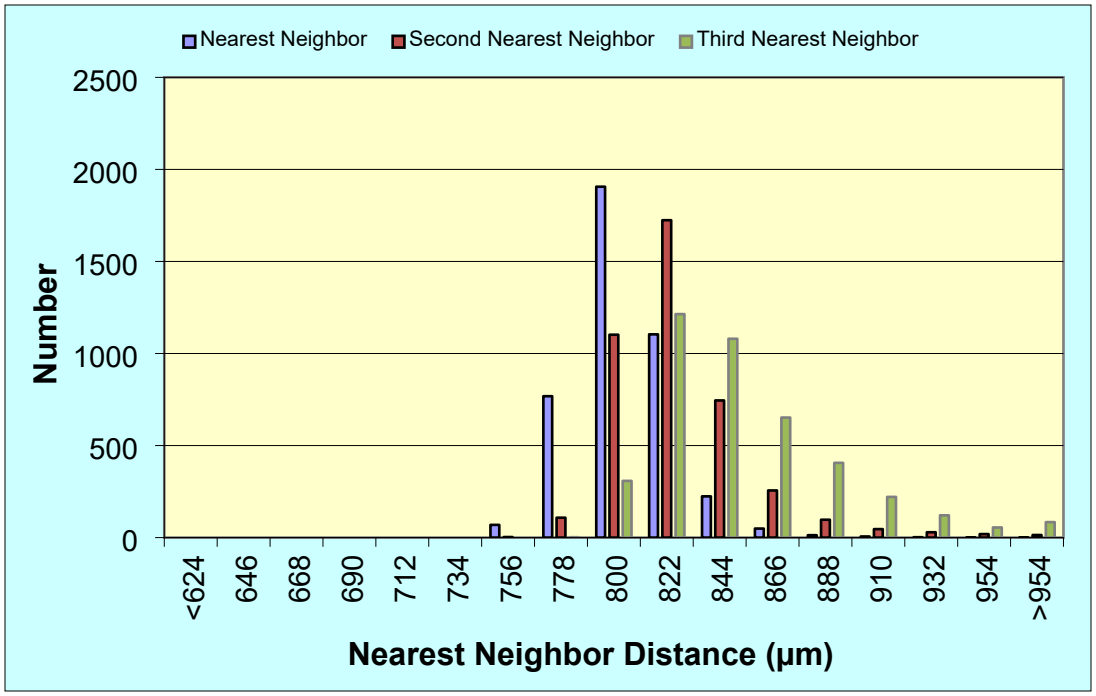

Figure 8. Nearest-neighbor distances for particles in LEU01-46T-47.

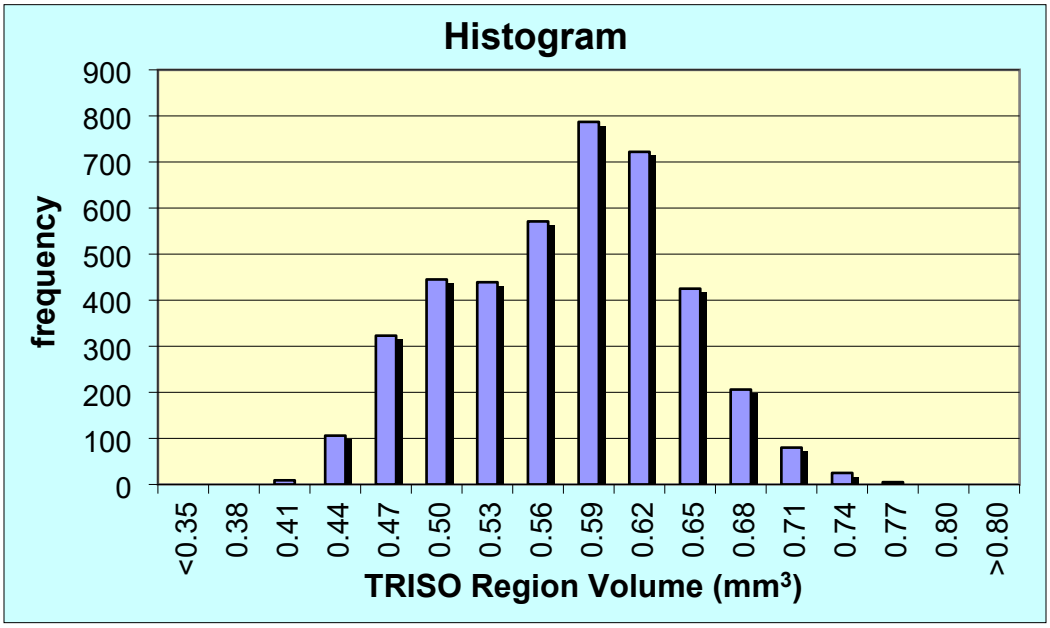

Figure 9. Region volumes of particles and surrounding matrix for particles in LEU01-46T-Z47.

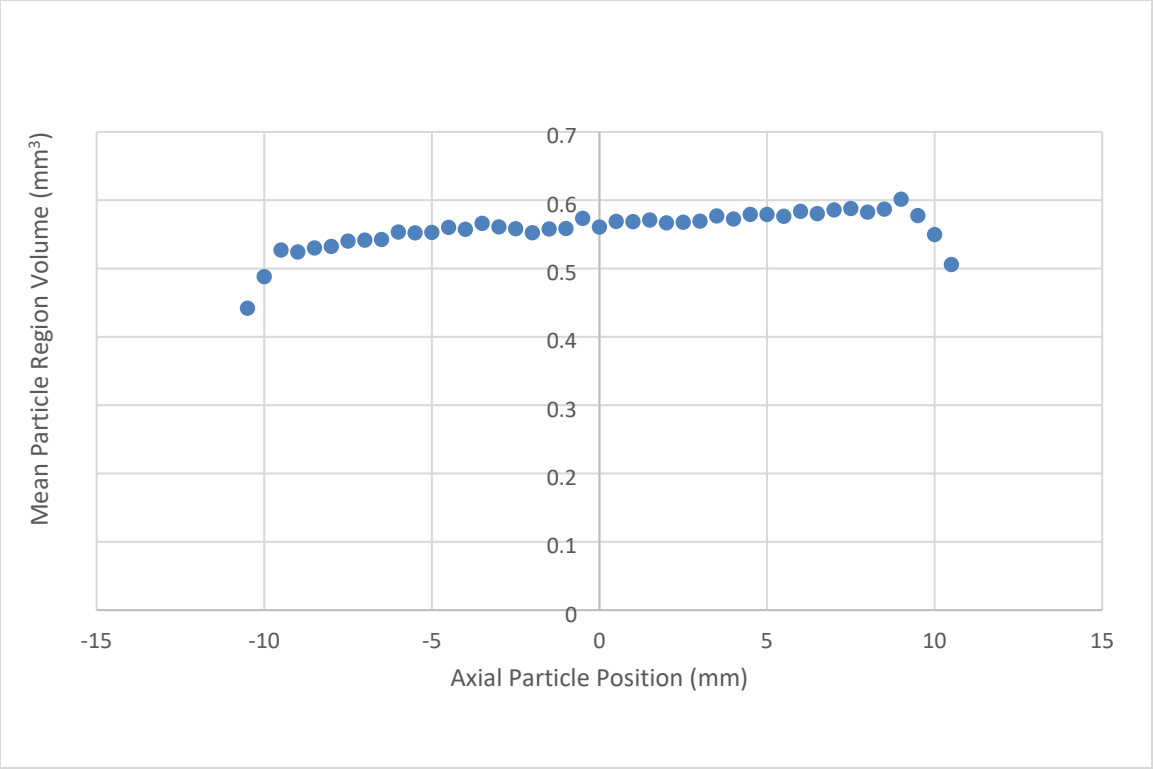

Figure 10. Mean region volume as a function of axial position within compact LEU01-46T-Z47.

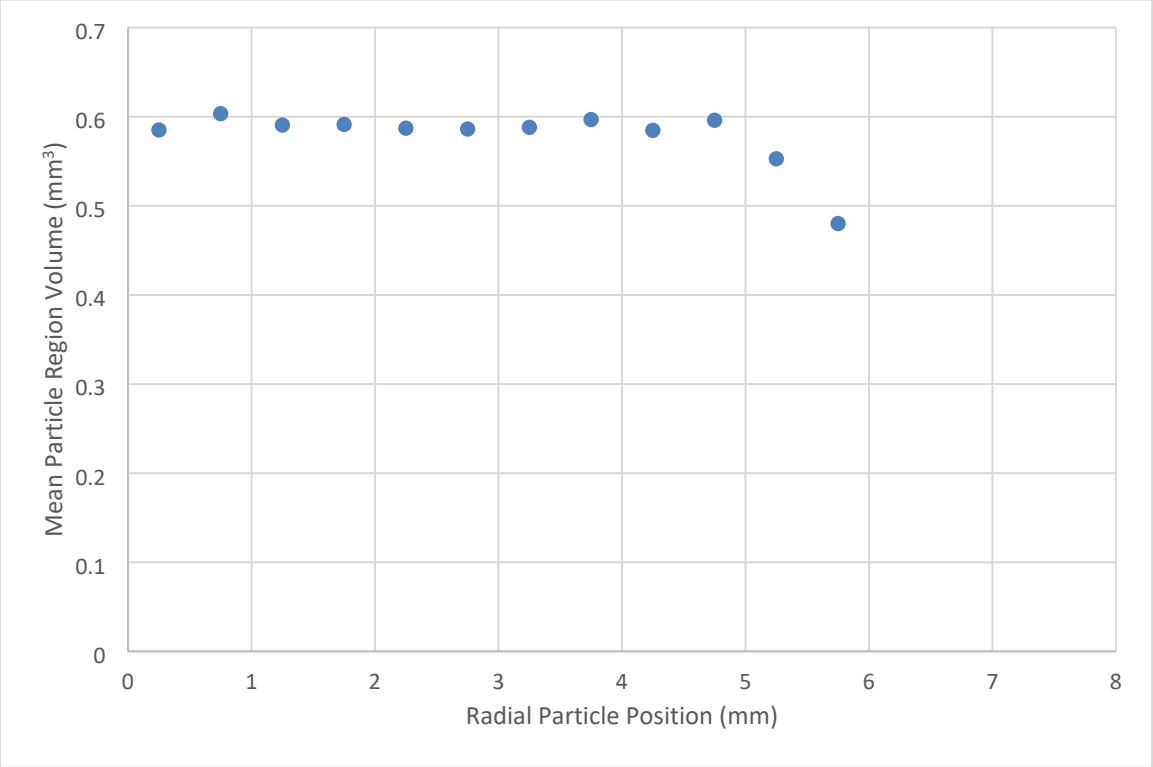

Figure 11. Mean region volume as a function of radial position within compact LEU01-46T-Z47.

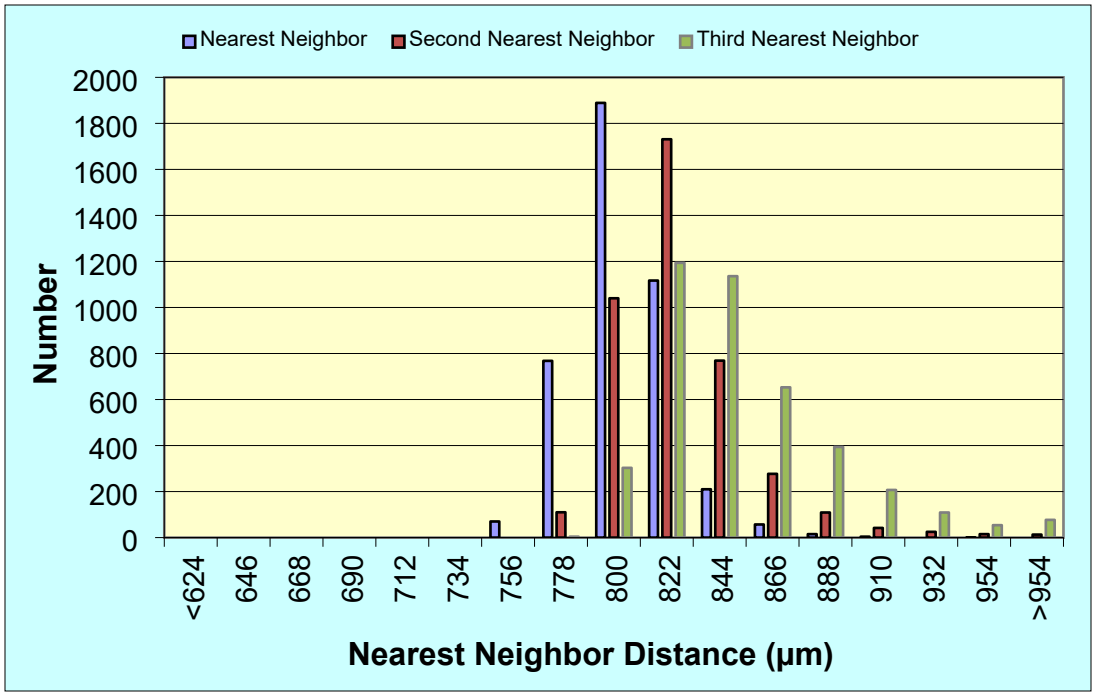

Figure 12. Nearest-neighbor distances for particles in LEU01-46T-Z68.

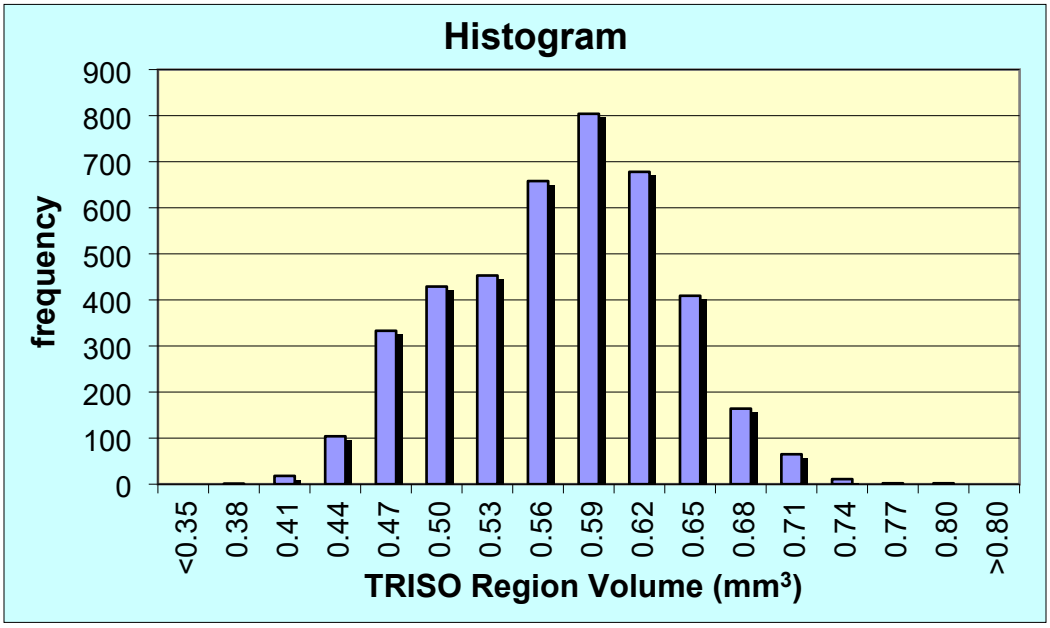

Figure 13. Region volumes of particles and surrounding matrix for particles in LEU01-46T-Z68.

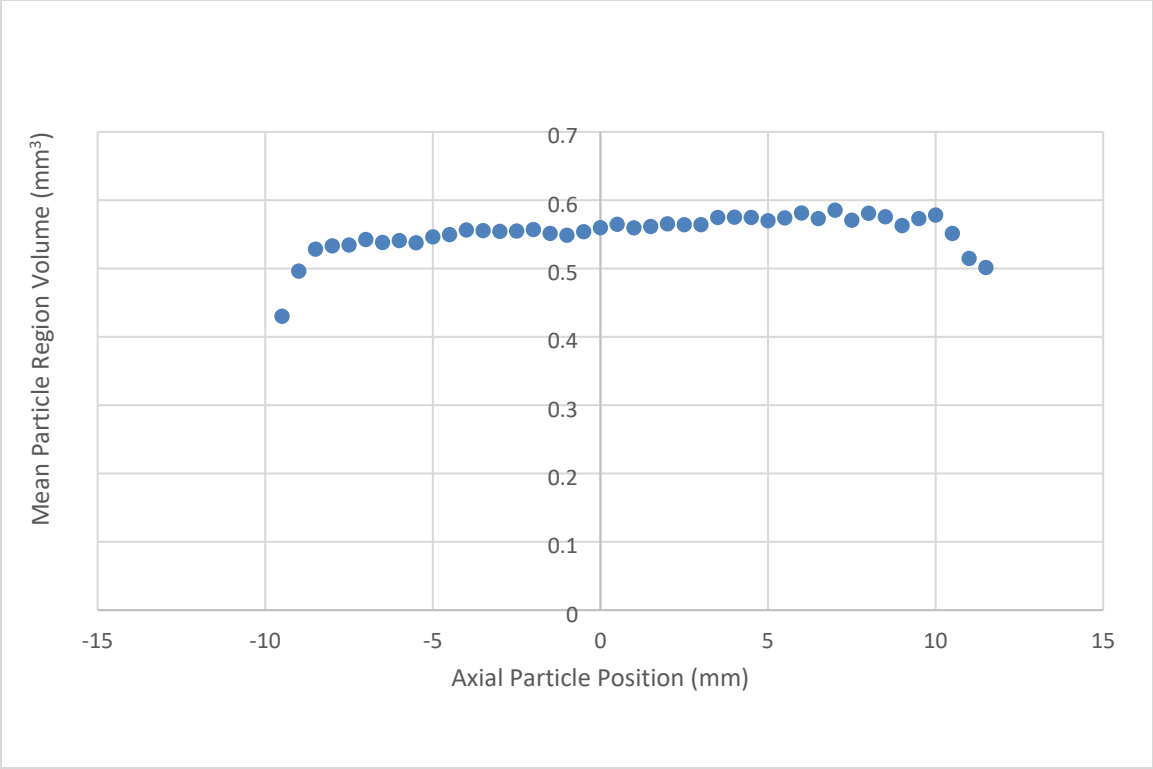

Figure 14. Mean region volume as a function of axial position within compact LEU01-46T-Z68.

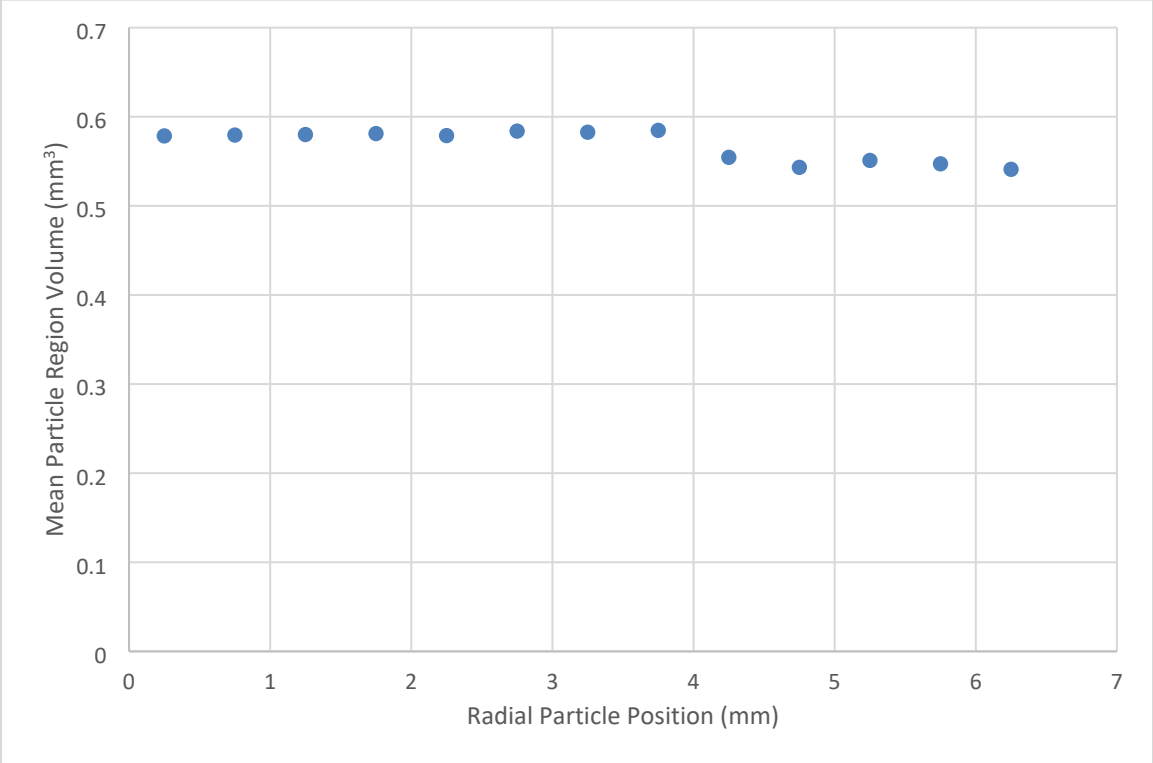

Figure 15. Mean region volume as a function of radial position within compact LEU01-46T-Z68.

APPENDIX B: PARTICLE DATA FROM AGR-2 UCO COMPACT XCT SCANS

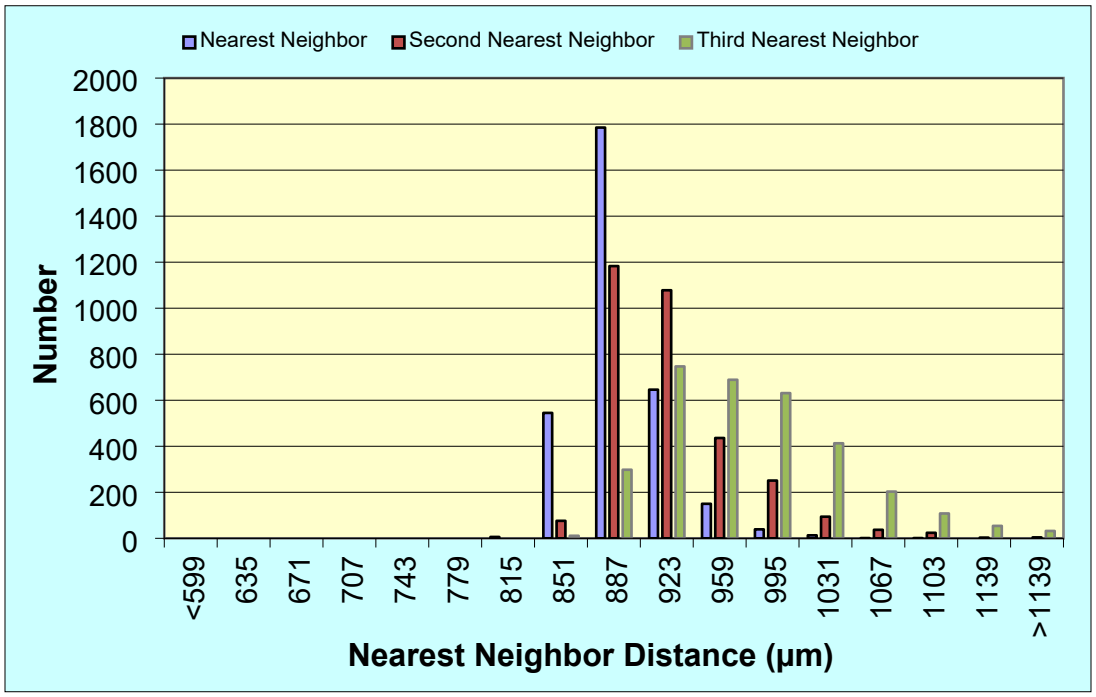

Figure 16. Nearest-neighbor distances for particles in LEU09-OP2-Z069.

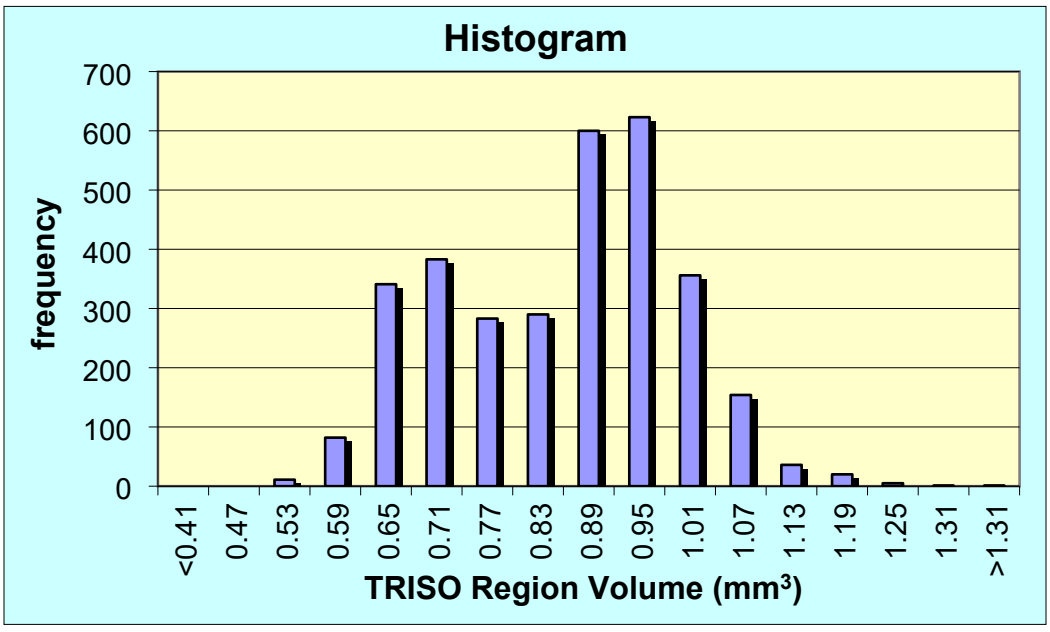

Figure 17. Region volumes of particles and surrounding matrix for particles in LEU09-OP2-Z069.

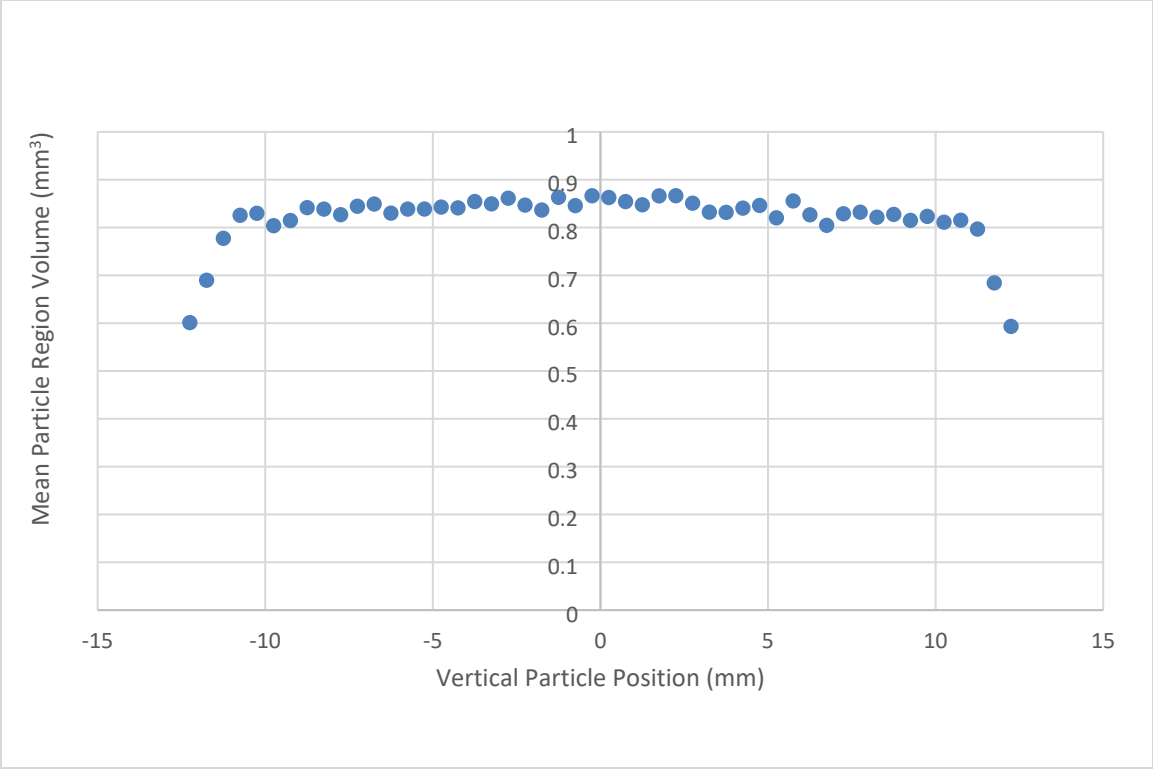

Figure 18 . Mean region volume as a function of axial position within compact LEU09-OP2-Z069.

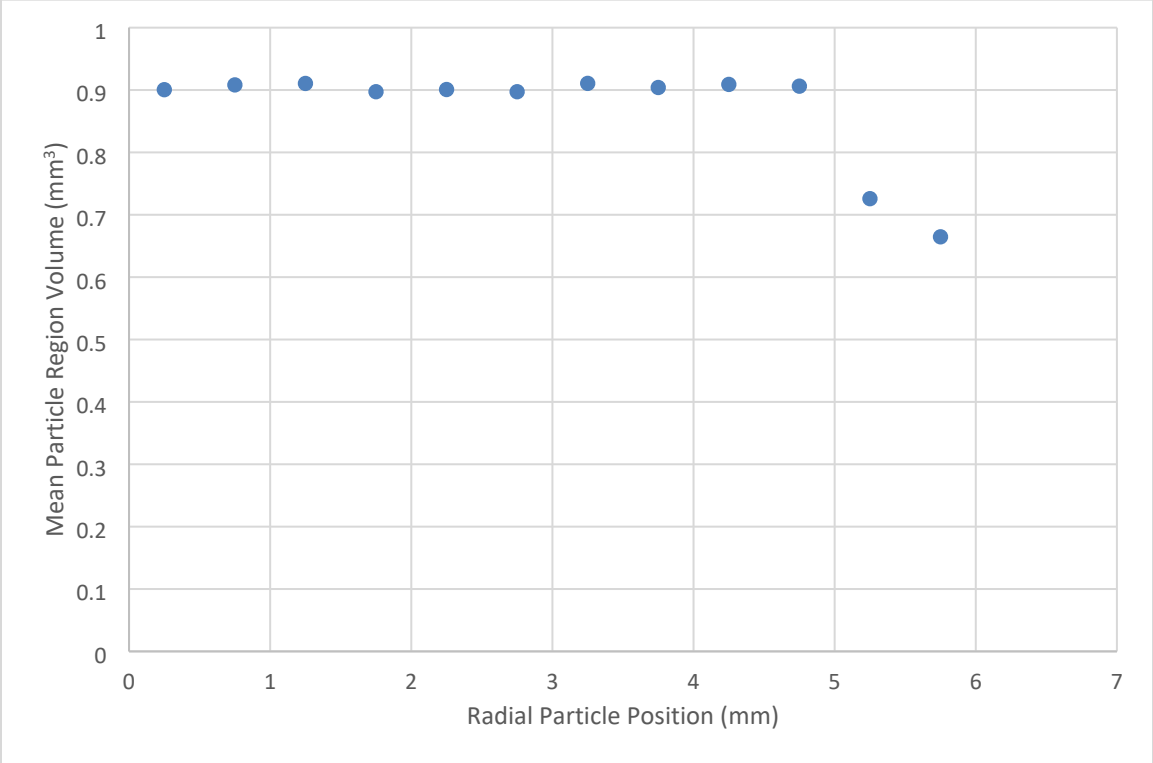

Figure 19 . Mean region volume as a function of radial position within compact LEU09-OP2-Z069.

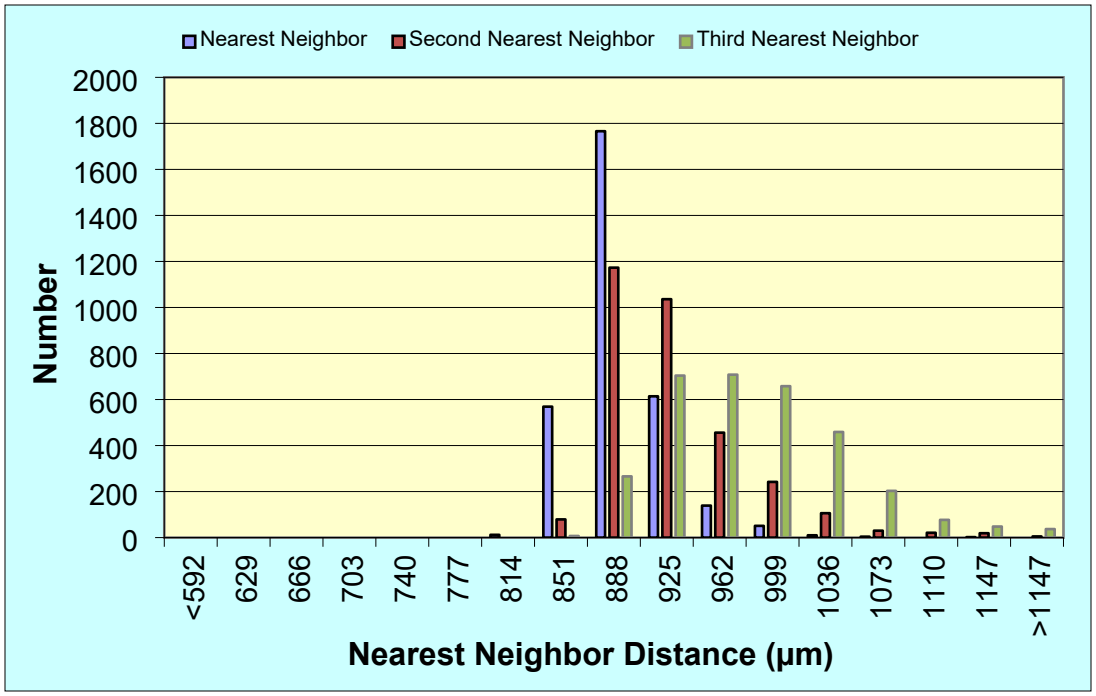

Figure 20 . Nearest-neighbor distances for particles in LEU09-OP2-Z102.

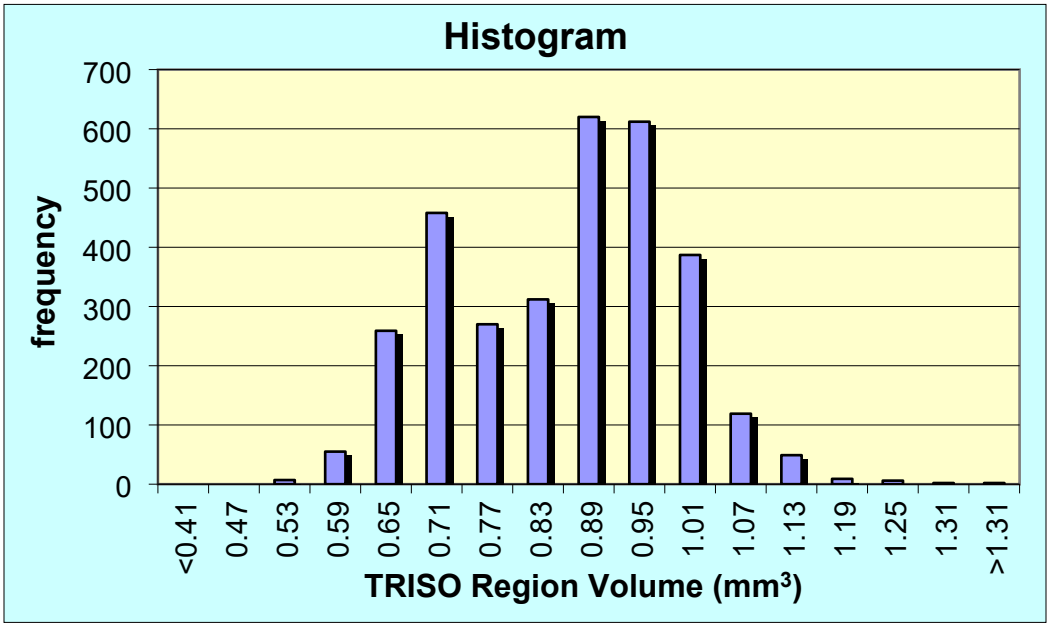

Figure 21 . Region volumes of particles and surrounding matrix for particles in LEU09-OP2-Z102.

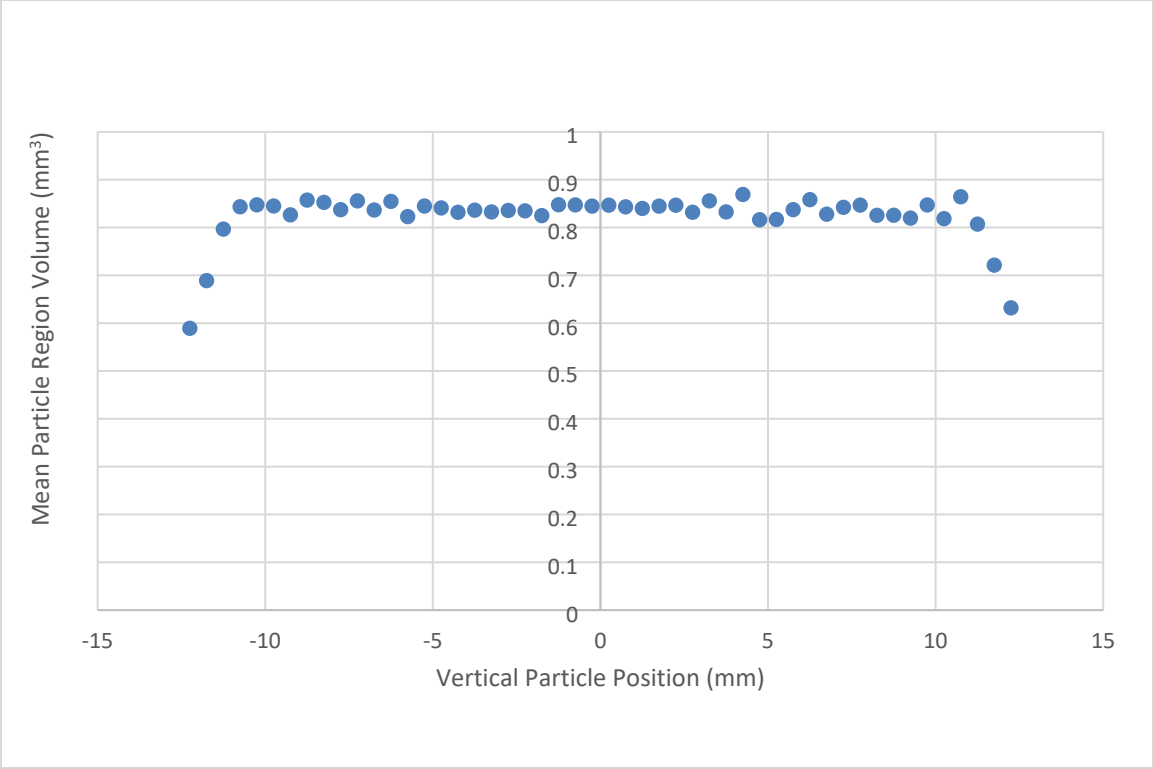

Figure 22 . Mean region volume as a function of axial position within compact LEU09-OP2-Z102.

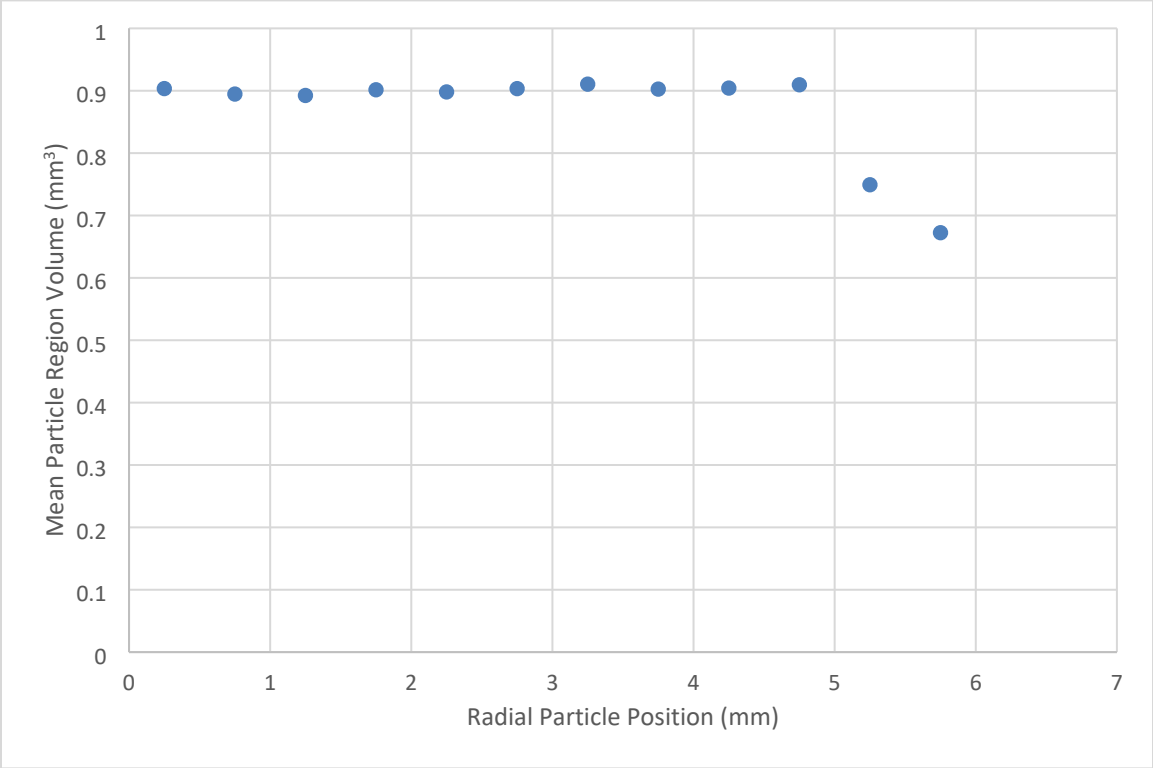

Figure 23 . Mean region volume as a function of radial position within compact LEU09-OP2-Z102.

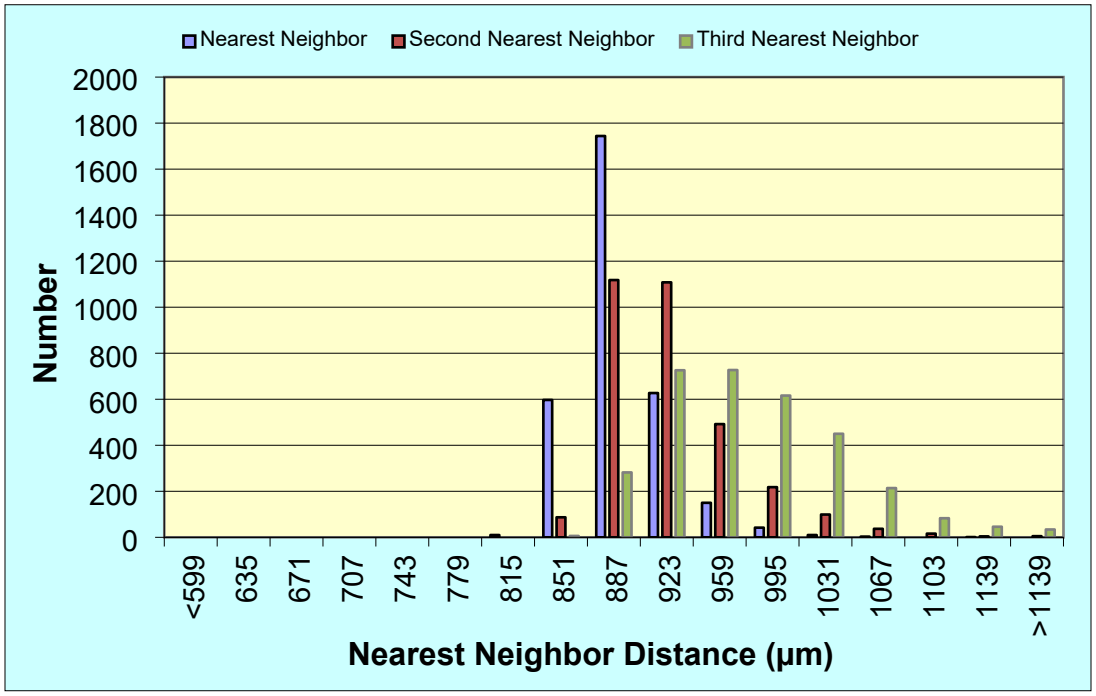

Figure 24 . Nearest-neighbor distances for particles in LEU09-OP2-Z139.

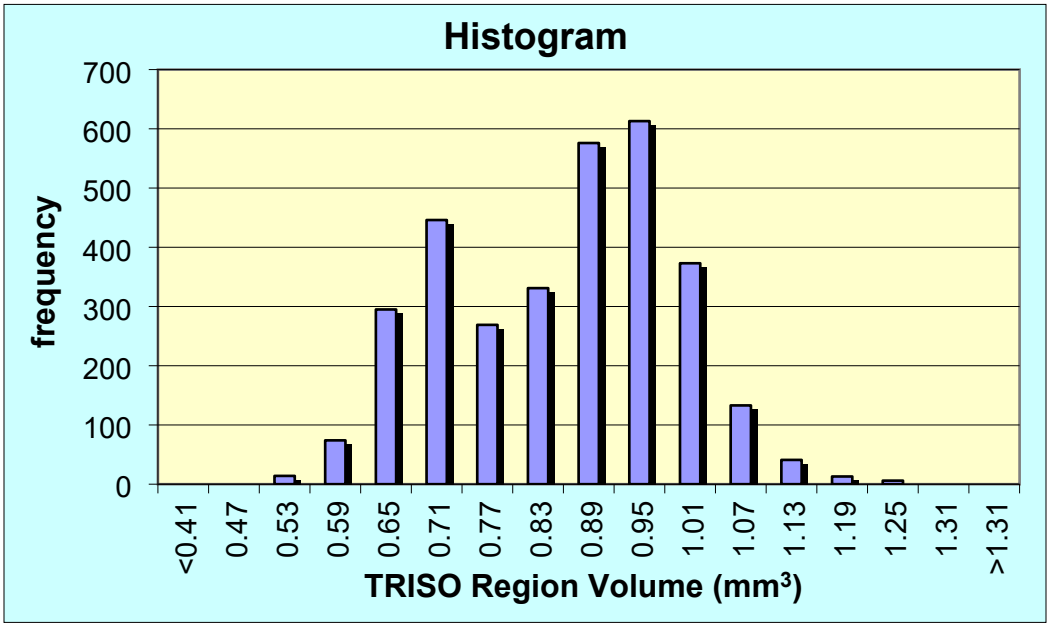

Figure 25 . Region volumes of particles and surrounding matrix for particles in LEU09-OP2-Z139.

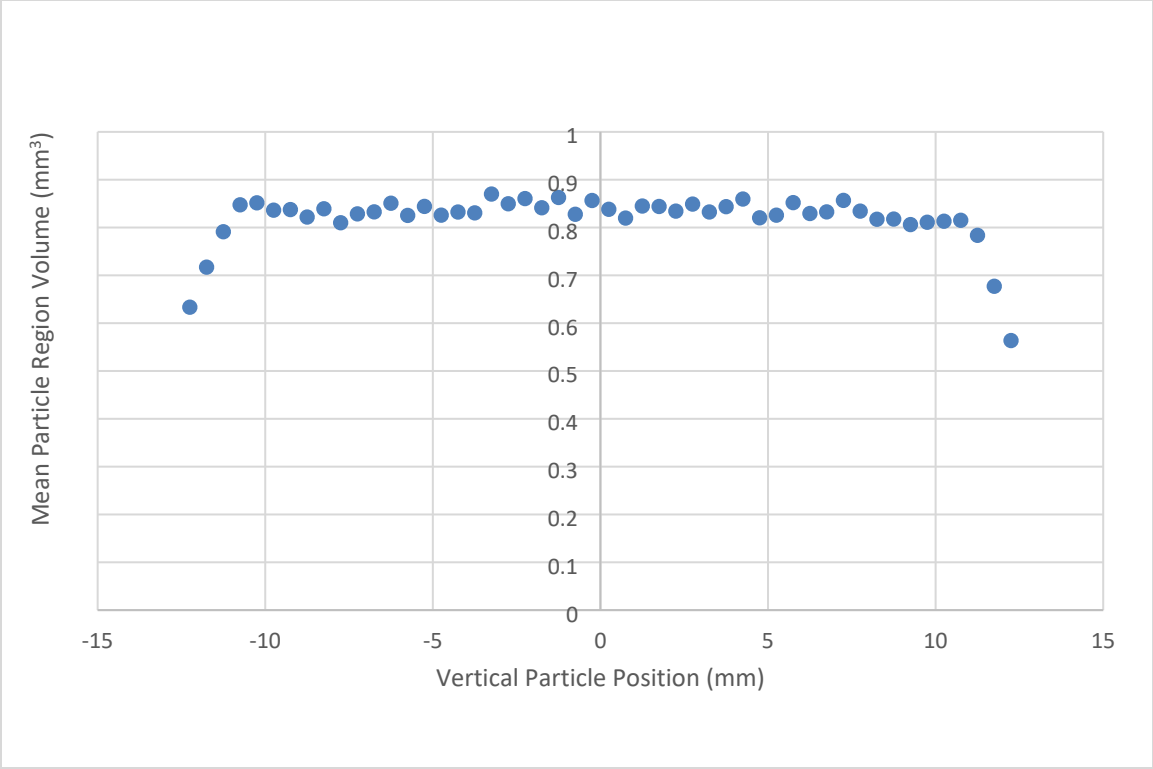

Figure 26 . Mean region volume as a function of axial position within compact LEU09-OP2-Z139.

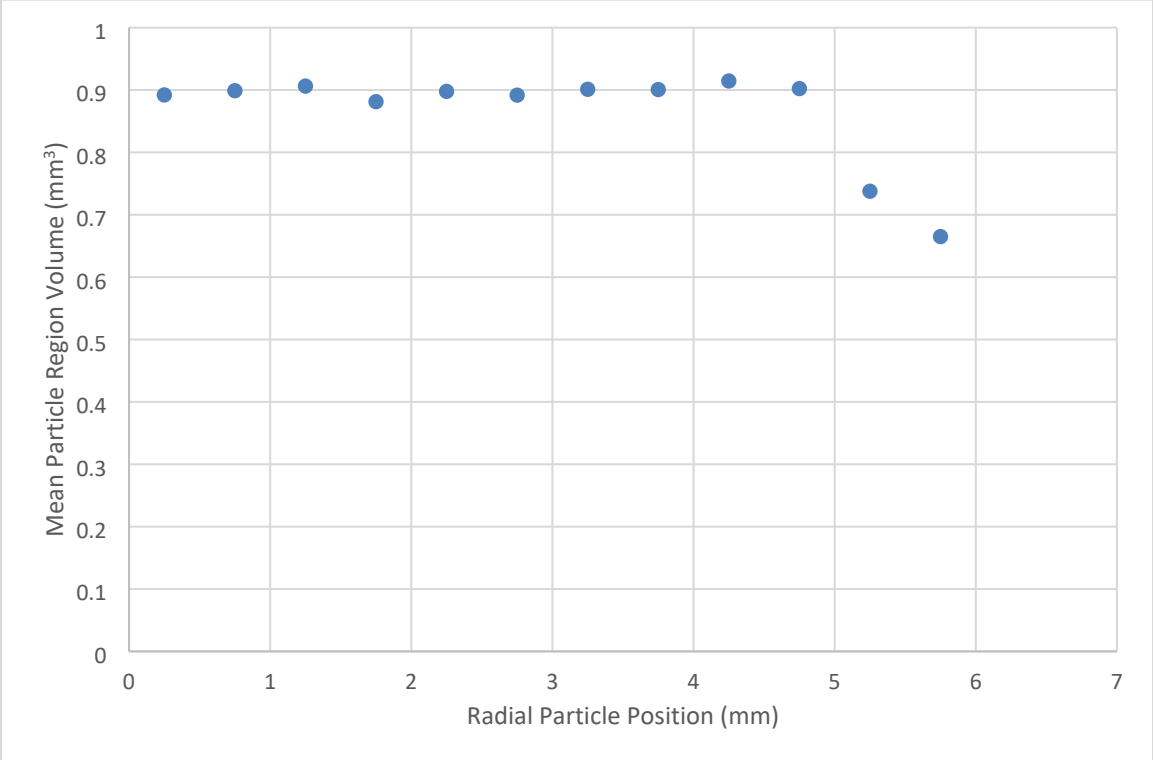

Figure 27 . Mean region volume as a function of radial position within compact LEU09-OP2-Z139.

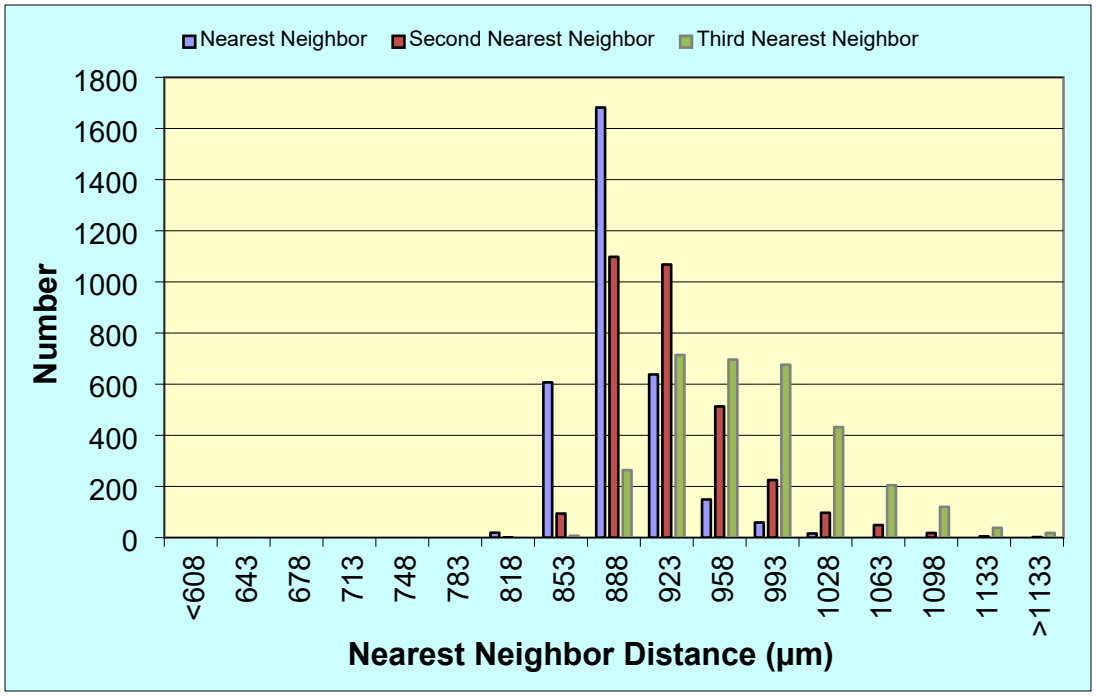

Figure 28 . Nearest-neighbor distances for particles in LEU09-OP2-Z165.

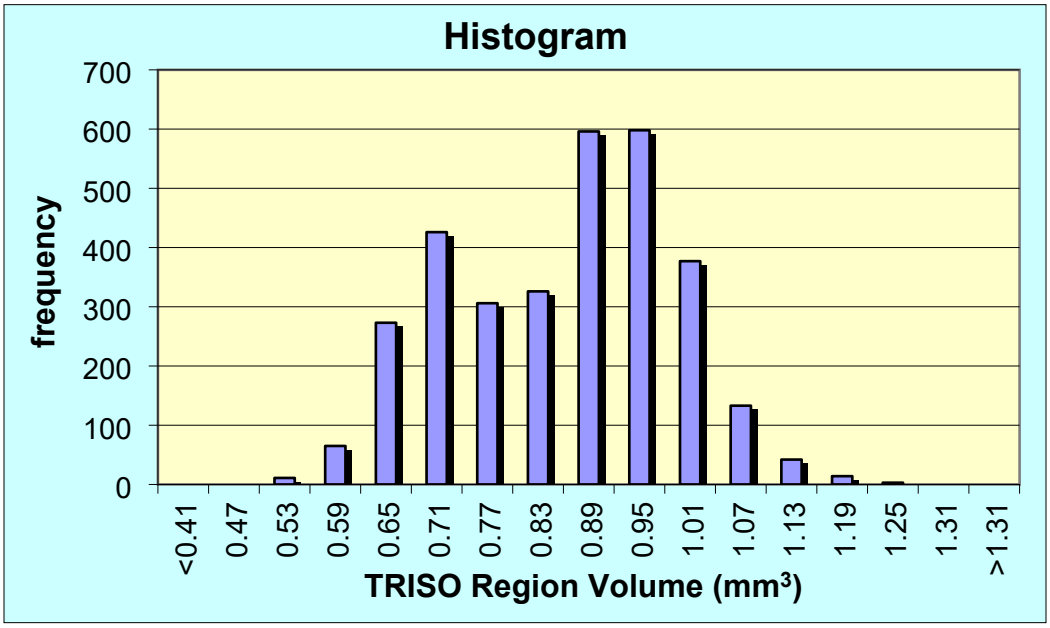

Figure 29 . Region volumes of particles and surrounding matrix for particles in LEU09-OP2-Z165.

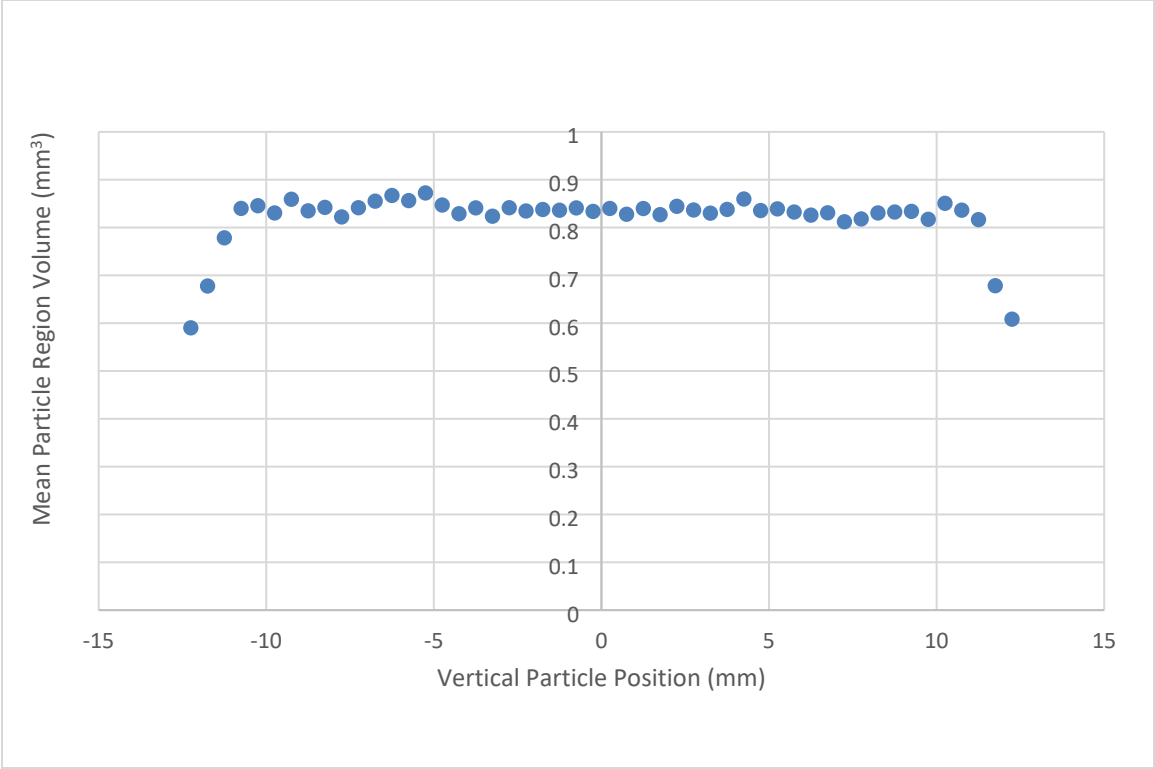

Figure 30 . Mean region volume as a function of axial position within compact LEU09-OP2-Z165.

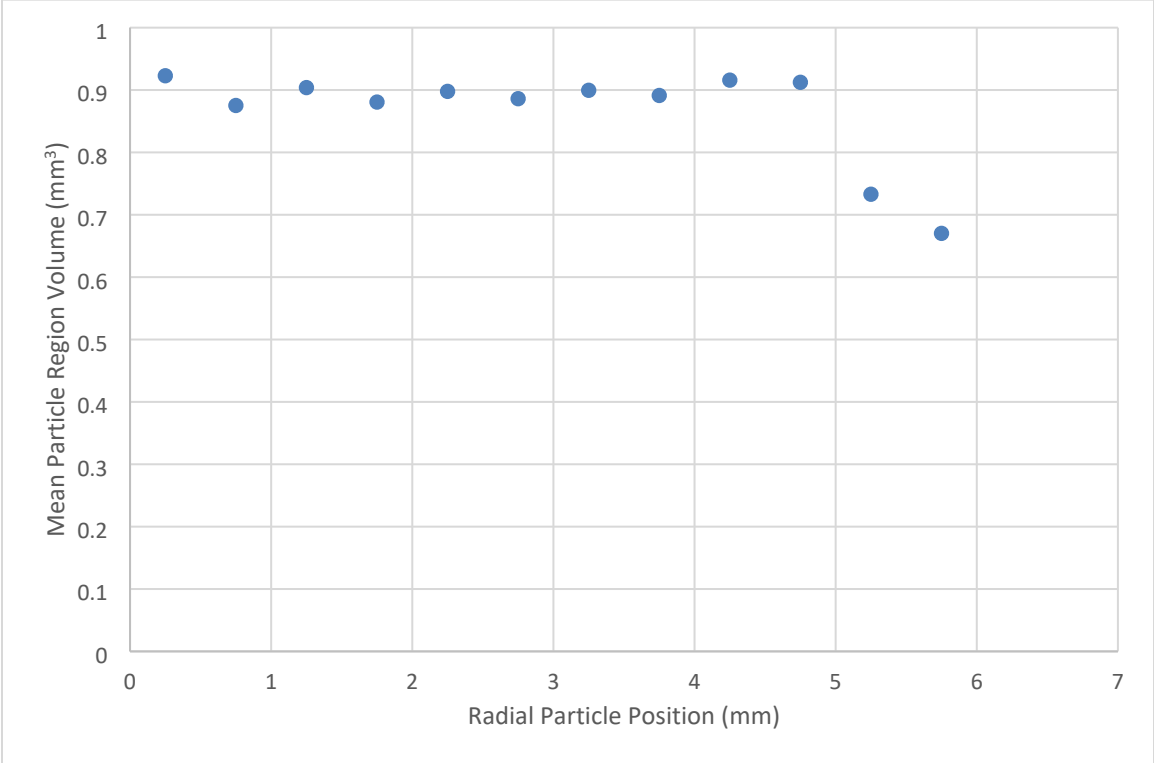

Figure 31 . Mean region volume as a function of radial position within compact LEU09-OP2-Z165.

APPENDIX C: PARTICLE DATA FROM AGR-2 UO_2 COMPACT XCT SCANS

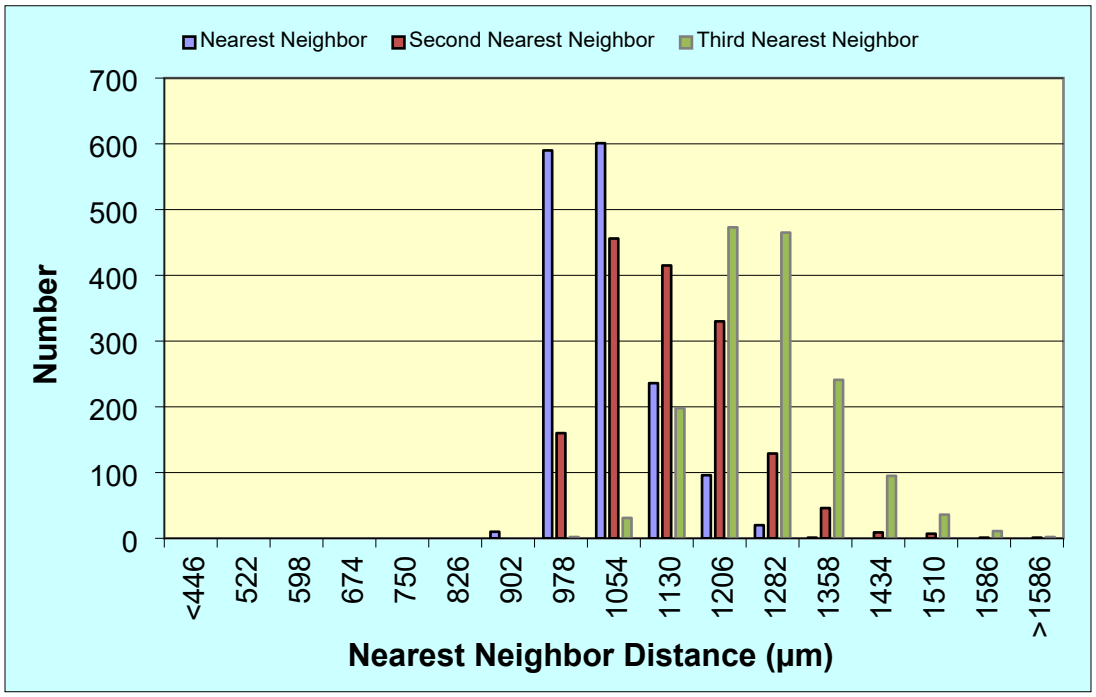

Figure 32 . Nearest-neighbor distances for particles in LEU11-OP2-Z045.

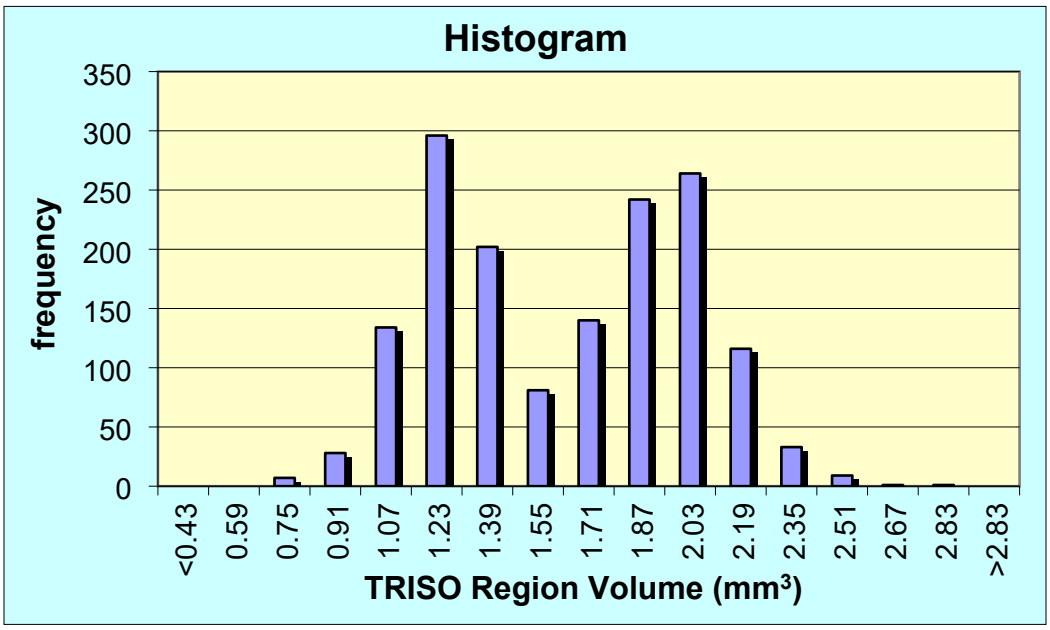

Figure 33 . Region volumes of particles and surrounding matrix for particles in LEU11-OP2-Z045.

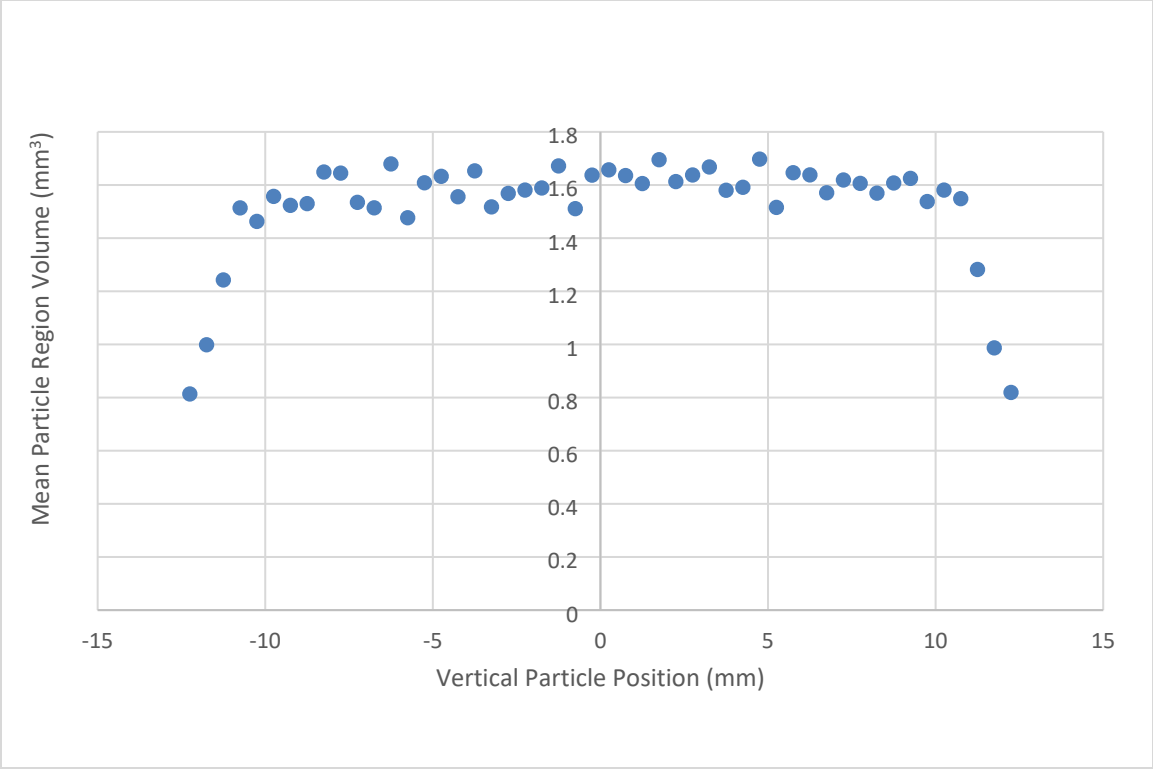

Figure 34 . Mean region volume as a function of axial position within compact LEU11-OP2-Z045.

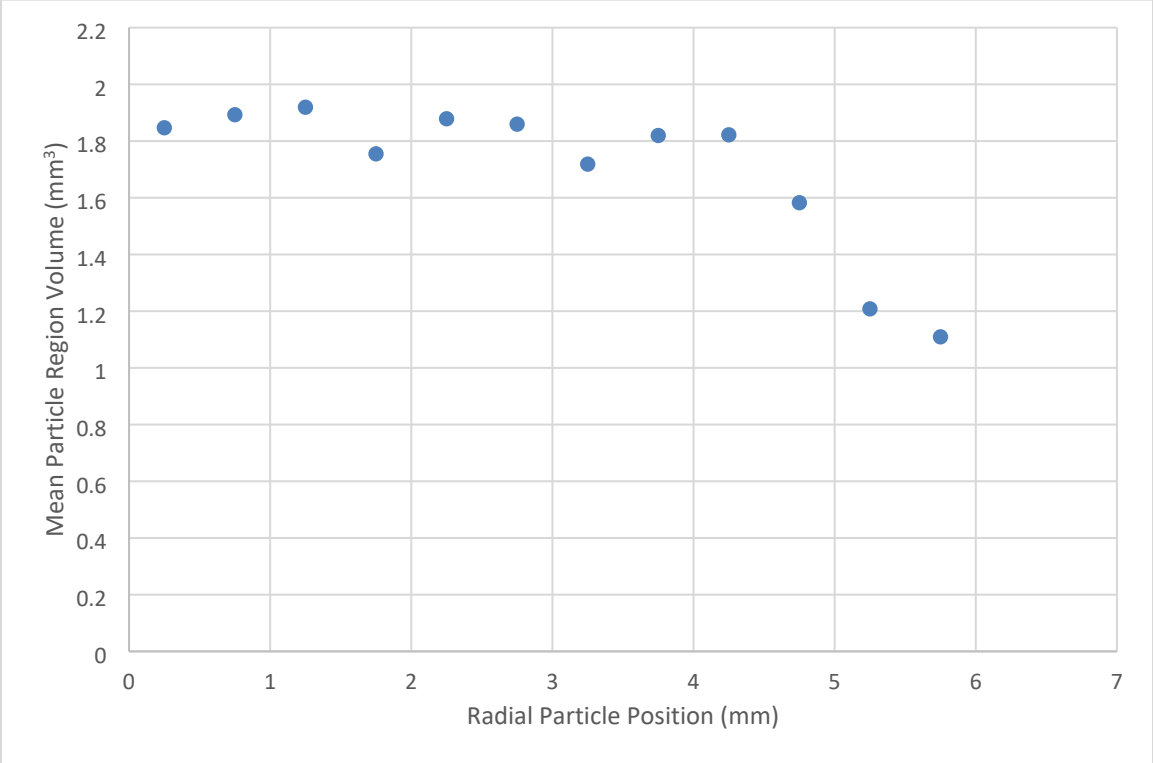

Figure 35 . Mean region volume as a function of radial position within compact LEU11-OP2-Z045.

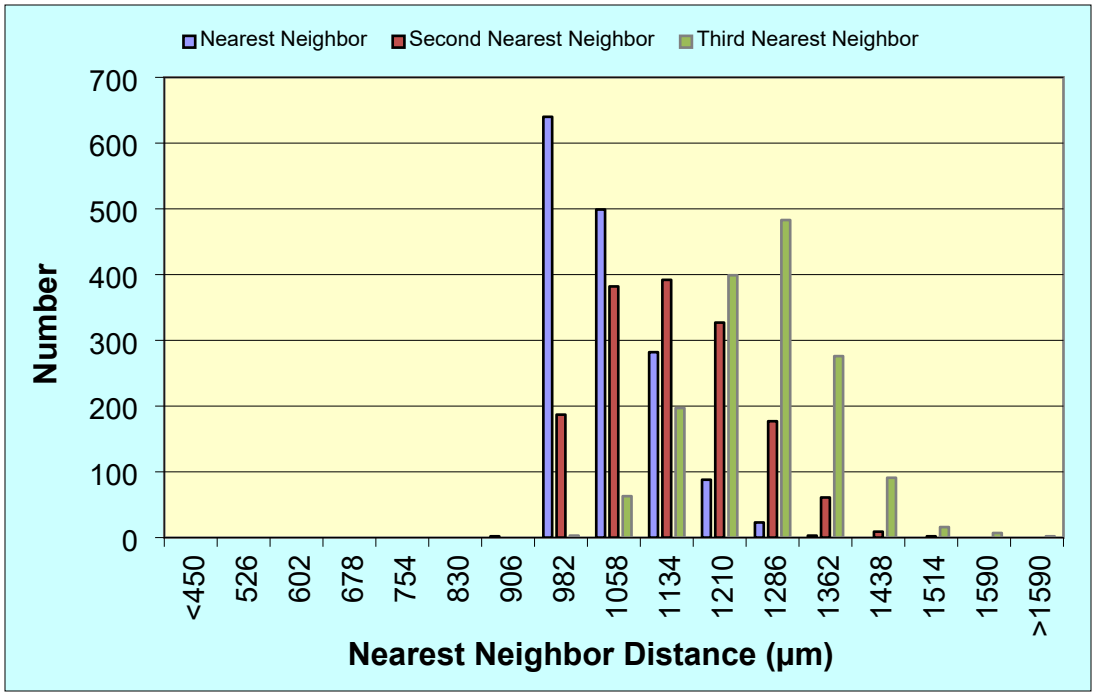

Figure 36 . Nearest-neighbor distances for particles in LEU11-OP2-Z074.

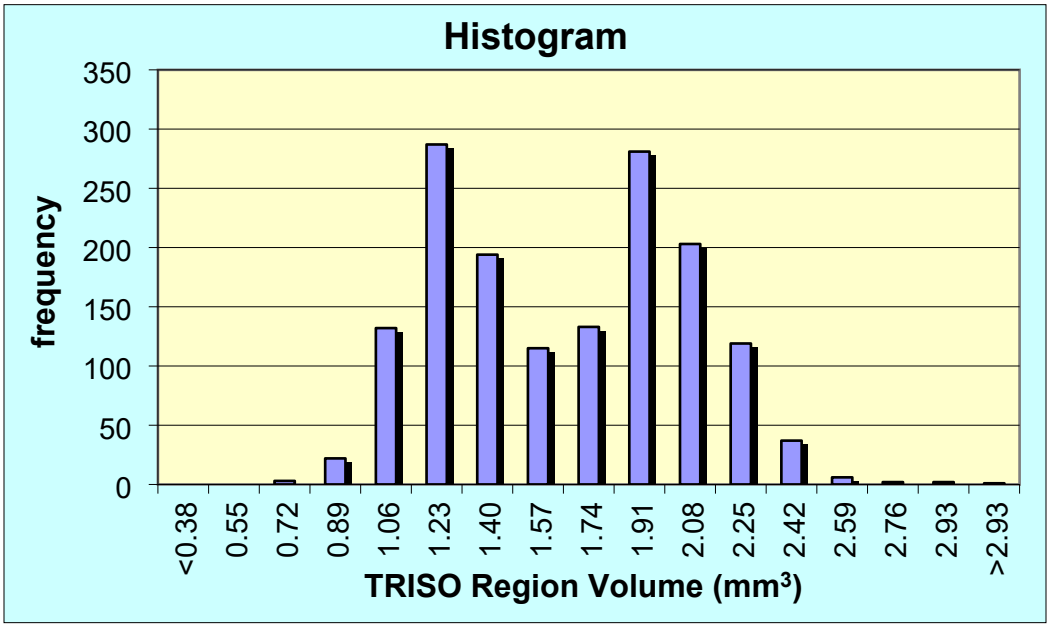

Figure 37 . Region volumes of particles and surrounding matrix for particles in LEU11-OP2-Z074.

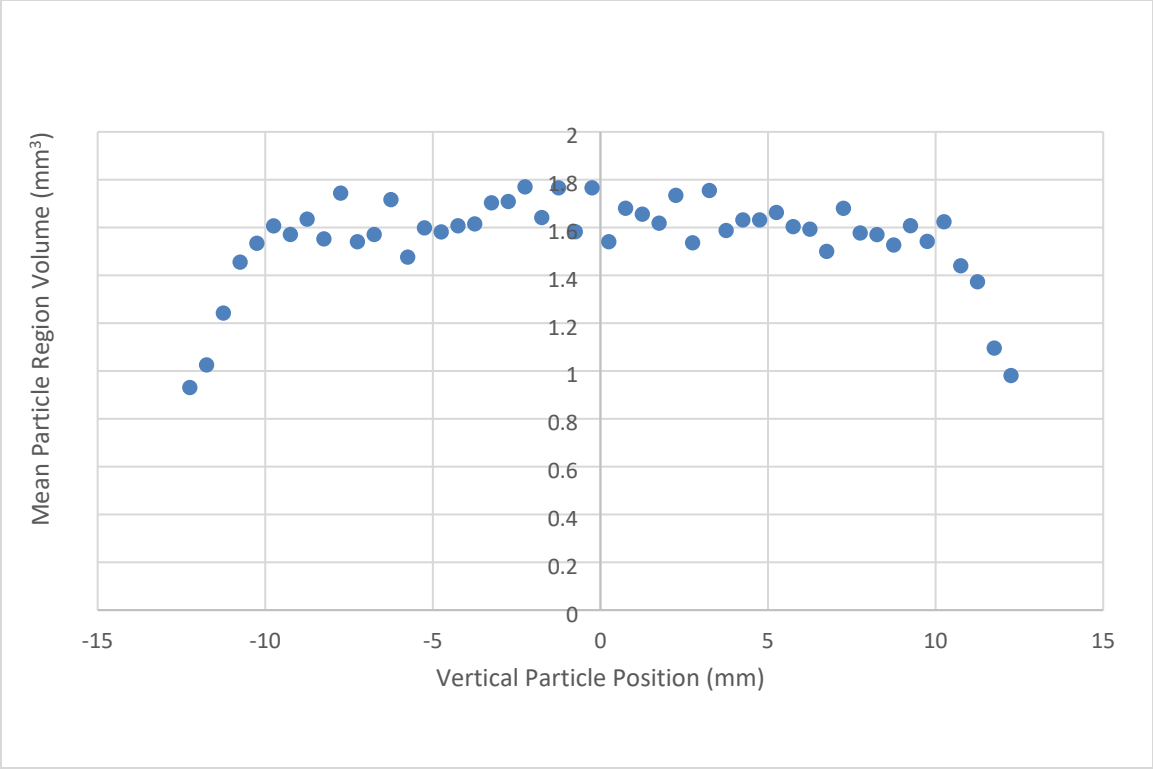

Figure 38 . Mean region volume as a function of axial position within compact LEU11-OP2-Z074.

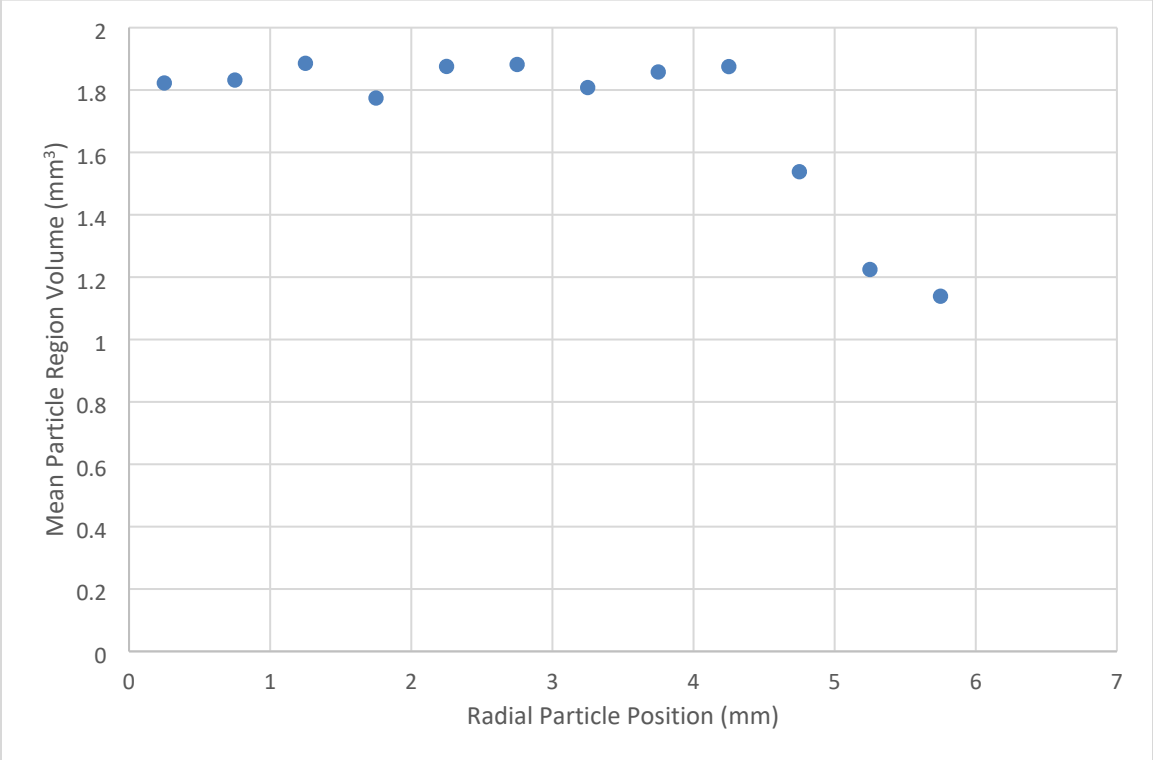

Figure 39 . Mean region volume as a function of radial position within compact LEU11-OP2-Z074.

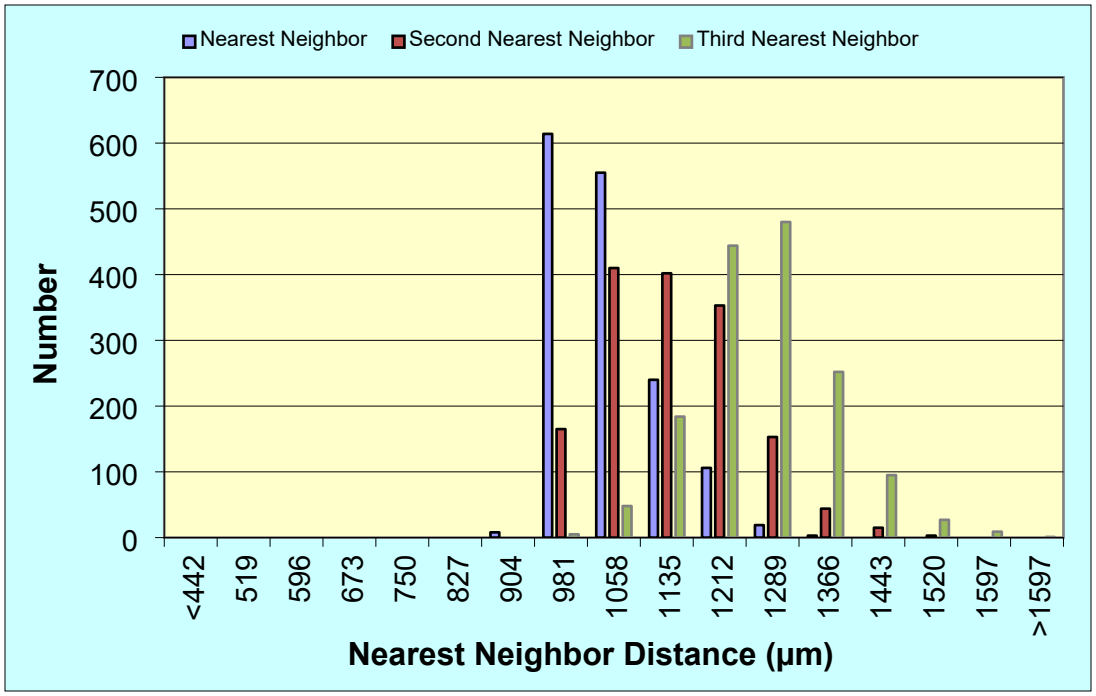

Figure 40 . Nearest-neighbor distances for particles in LEU11-OP2-Z198.

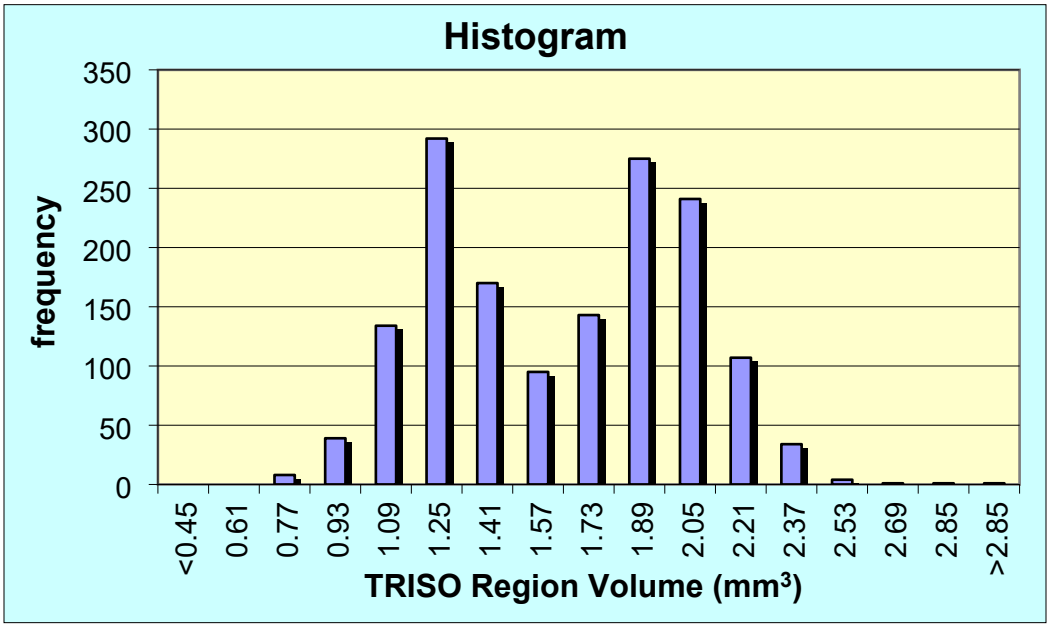

Figure 41 . Region volumes of particles and surrounding matrix for particles in LEU11-OP2-Z198.

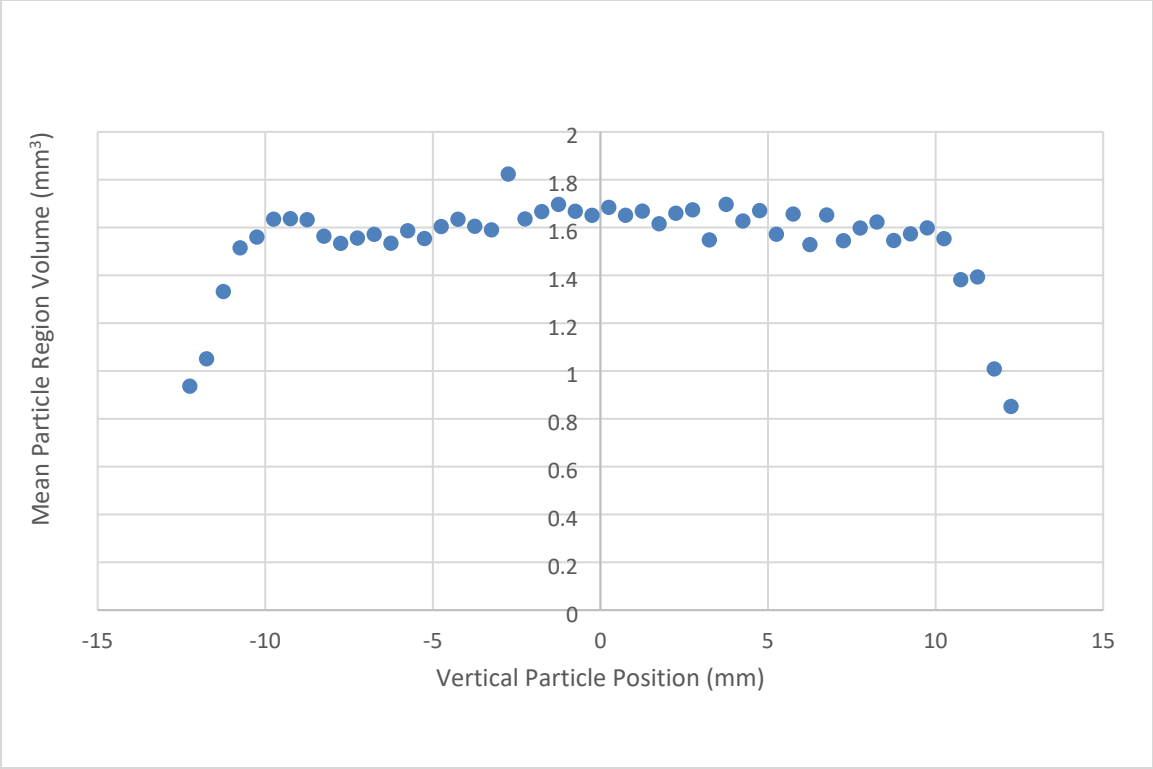

Figure 42 . Mean region volume as a function of axial position within compact LEU11-OP2-Z198.

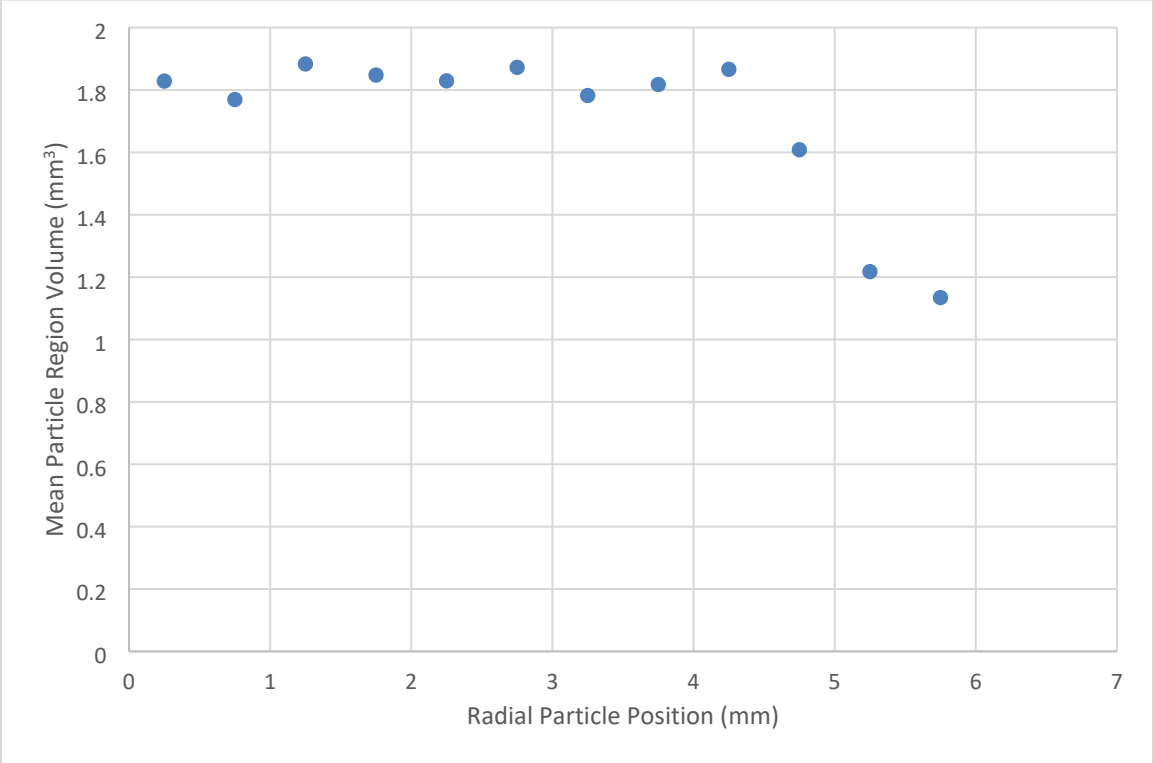

Figure 43 . Mean region volume as a function of radial position within compact LEU11-OP2-Z198.